ACOUSTIC POWER TRANSFER SYSTEMS FOR IMPLANTABLE MEDICAL DEVICES: MODELING TECHNIQUE AND ANALYSIS

by

David Brent Christensen

A dissertation submitted to the faculty of
The University of Utah
in partial fulfillment of the requirements for the degree of

Doctor of Philosophy

Department of Mechanical Engineering

The University of Utah

December 2017

The University of Utah Graduate School

STATEMENT OF DISSERTATION APPROVAL

The dissertation of **David Brent Christensen**

has been approved by the following supervisory committee members:

Shadrach J. Roundy	, Chair	**8/16/2017** Date Approved
Brittany Coats	, Member	**8/16/2017** Date Approved
Robert B. Roemer	, Member	**8/16/2017** Date Approved
Bruce K. Gale	, Member	**8/16/2017** Date Approved
Allison Hampshire Payne	, Member	**8/16/2017** Date Approved

and by **Timothy A. Ameel** , Chair/Dean of

the Department/College/School of **Mechanical Engineering**

and by David B. Kieda, Dean of The Graduate School.

ABSTRACT

Implantable medical devices (IMDs) are small devices that can be implanted into biological tissue to perform a diagnostic or therapeutic function. In this work, acoustic power transfer (APT) is investigated to wirelessly power IMDs. Acoustic power transfer systems (APTS) are typically comprised of an electrical source, acoustic transmitter (TX), medium through which the acoustic waves propagate, acoustic receiver (RX), and electrical load. The source powers the TX that emit acoustic waves through the medium to power the RX. The electrical load is attached to the RX and represents the IMD sensing or actuation system with associated electronics. In this work, the bulk-mode piezoelectric plate and flexure-mode piezoelectric diaphragm are considered for the acoustic TX and RX. A comparative study of power transfer potential (PTP) of the plate and diaphragm as a function of size and depth found that the diaphragm has higher PTP at submillimeter device sizes, the plate and diaphragm have comparable PTP at low-millimeter sizes, and the plate has higher PTP at larger sizes. Current modeling techniques for APTS include use of basic equations, circuit equivalent models, Huygens principle, two-dimensional (2D) axisymmetric finite-element analysis (FEA), and three-dimensional (3D) FEA. These techniques are used to model the PTP of the APTS in terms of electrical load, frequency, depth, and transducer diameter. Although researchers acknowledge that the orientation and alignment of the RX relative to the TX play a significant role in power transfer, none of the modeling techniques employed, except 3D FEA, are able to model these effects and 3D

FEA is generally not employed because of its steep computational cost. This research develops a modeling technique that is capable of modeling Depth, Orientation, and Alignment via Ray Tracing (DOART) and is one to two orders of magnitude faster than 3D FEA. DOART is used to explore PTP sensitivity to disturbances in RX depth, orientation, and alignment. Four types of design graphs are developed to aid designers in the selection of APTS parameters such as TX and RX diameter, frequency, and depth. These design graphs are generated using nondimensional parameters to broaden their applicability and provide insight into scaling.

For Krystal, who does the real work behind the scenes.

TABLE OF CONTENTS

LIST OF TABLES

Tables

ACKNOWLEDGMENTS

Special thanks goes to my advisor, Dr. Shad Roundy, for his tremendous support and mentoring over these past years. Thanks also goes to Doug Christensen for his excellent teaching of ultrasound theory, Hamid Basaeri for his assistance with experimental and finite-element modeling work, and Dean Constantine who provided practical experience with various types of ultrasonic transducers to compliment my theoretical training. Continual support from my family has made this work possible.

Financial support for this work was provided by the National Science Foundation through grant number ECCS 1408265.

CHAPTER 1

INTRODUCTION

1.1 Implantable Medical Devices

Implantable medical devices (IMDs) have gained interest over the past decade with advances in power electronics, sensing, complimentary metal-oxide semiconductors (CMOS), and communications technology. IMDs are small devices, on the mm to cm scale, which can be implanted into biological tissue to perform a therapeutic or diagnostic function. An example of an IMD is the CardioMEMS HF System which was approved by the United States Food and Drug Administration (FDA) in 2014. This device allows doctors to wirelessly monitor the cardiac filling pressure in patients with heart failure and respond accordingly with adjustments in medication. A clinical trial reported that heart failure management resulting from the device was associated with a 28% decrease in hospitalizations during a 6-month period and a 37% decrease over a 15-month period [1]. The device is about the size of a small paper clip and is inserted into the pulmonary artery via catheter making implantation significantly less traumatic to the body than insertion via surgery. The device does not have a battery. Rather, the patient powers the device at regular intervals via electromagnetic induction by placing a coil over the implant area. The coil powers the implant and collects systolic, diastolic and mean pressure readings. These readings are sent back to the physician for monitoring and medication adjustments as necessary [2].

Another application of IMDs is glucose sensing [3][4]. Currently, patients who have diabetes prick their finger to draw blood in order to test glucose levels. A miniature glucose IMD would allow patients to obtain glucose levels without having to prick their finger. Similar to the CardioMEMS HF system, the patient would power the device at regular intervals using wireless power transfer. The glucose readings would be available for the patient to view and store in their personal health file and/or send to a physician. This type of device would significantly increase the ease of obtaining glucose levels and the comfort of the patient. IMDs that are either futuristic or under development range in function from drug delivery and therapeutic, such as electrostimulation treatments that aid in treating Parkinson’s disease, epilepsy, depression, heart failure, and chronic pain [5], nerve cuff stimulators [6], optogenetic stimulators [7], [8], and micro oxygen generators [9], to diagnostic, such as measuring blood glucose, blood pressure, bladder pressure [10], and doppler blood flowmeters for post microvascular free flap surgery to check for anastomotic failure [11]. Work is also being done in the area of neural prosthetic systems [12]–[14]. These types of IMDs are of interest to patients because they can provide preventative, remote, and personalized health care. Their use is becoming even more beneficial with the recent explosive growth in the usage of mobile health apps and health monitoring devices paired with smartphones and tablets [15]. Minimally invasive or non-surgical implantation is a particularly desirable feature of IMDs to minimize patient trauma. To provide this feature, the IMD must be small while still being able to provide sufficient power to the electronics and sensors.

1.2 Powering Methods

Batteries are the traditional method of powering wireless devices. However, as IMD sizes get smaller, battery sizes must also get smaller. The smallest batteries commercially available from Panasonic are a rechargeable lithium manganese coin cell battery (4.8 mm diameter, 2.1 mm height, 2.3 mAh at 3 V) and a rechargeable Li-ion pin battery (3.6 mm diameter, 20 mm height, 13 mAh at 3.75 V) [16]. The calculated energy volume density for each of these batteries is 0.1816 mWh/mm^3 and 0.2395 mWh/mm^3 respectively. If a miniature IMD allowed for a 1 mm^3 battery volume, and this size of battery were manufacturable, the total available energy for the IMD could be estimated to be between 0.1816 mWh to 0.2395 mWh (this type of linear scaling is probably an overestimate as the required packaging material would probably occupy a higher percent of the total volume). IMD power requirements can range from a few μW [9] to a few mW [17]. If the IMD required 50 μW to operate, the battery would need to be recharged at least every 3.63 to 4.79 hours of operation. If a lithium primary battery were used, which has about twice the energy density than rechargeable lithium batteries, the battery would need to be replaced after 7.26 to 9.58 hours of operation. Replacing the battery is an option, but may require surgery. Surgery is traumatic to patients and can result in scars and complications such as hematoma formation for even the simplest of surgeries. Recharging the battery is an attractive option that could allow for prolonged device use after a recharging session. Preferably this would be done without the use of wires protruding through the skin. Removing the battery completely is also an attractive option that would allow IMDs to function only when being powered and could allow for further miniaturization of IMDs. The latter two options, which could avoid surgery to replace the battery, are the preferable solutions and could be accomplished via wireless power transfer technology.

Wireless power transfer methods include electromagnetic power transfer which can operate in the near-field, mid-field, or far-field, and acoustic power transfer (APT). Electromagnetic induction in the near-field (EMI) employs a transmitter (TX) and receiver (RX) coil that are inductively coupled. This method of power transfer has had commercial success, such as with the CardioMEMS HF System, but is not without its limitations. In [18], EMI is used to power a subretinal neurostimulator implanted in a Yucatan minipig eye. The paper reports that a 41.3-mm diameter TX power coil with a 27-mm diameter TX data coil and a 10.3-mm diameter RX power coil with a 7.6-mm RX data coil operating at 125 kHz for power and 15 MHz for data are used. Reliable data transfer is achieved through 22 mm of air (air is assumed as the paper did not specify), through 20 mm of biological saline in a benchtop test, and through 5 to 10 mm of orbital tissue. The differences are attributed to absorption in the tissue (tissue heating) and misalignment of the coils. Common concerns with EMI are reported in wireless power transfer review articles [19], [20] and include tissue absorption, power attenuation according the inverse cube of transmission distance, large coil size requirements, and high sensitivity to misalignment. EMI operates in the hundreds of kHz to tens of MHz range. Mid-field and far-field electromagnetic power transfer (RF) use TX and RX antennas to transfer power. These devices typically operate in the hundreds of MHz to low GHz range, do not require coils to be coupled, and are less sensitive to misalignment. However, they suffer from power regulations and high tissue absorption. The FCC imposes a maximum permissible RF exposure limit for humans in a controlled environment that is dependent on frequency in MHz [21]. For example, for frequencies in the range of 300 to 1500 MHz, the frequency in MHz is divided by 3 to obtain the maximum power density in mW/cm^2. From 1500 to 100000 MHz, the power density is 5 mW/cm^2. Instructions are given to average intensity readings over 6 minutes with a note that these limits are only suitable for far-field calculations. The guidelines set forth by the International Commission on Non-Ionizing Radiation Protection set the safe limit for whole-body electromagnetic radiation at 10 specific absorption rate (SAR) (W/kg) for occupational radiation and 2 SAR for public radiation between the frequencies of 100 kHz and 10 GHz [22]. These guidelines can be used for both EMI and RF. APT typically uses a piezoelectric TX and RX to transmit acoustic power through biological tissue and operates at frequencies in the hundreds of kHz to low MHz range. A comparative study of EMI and APT, [23], found that APT is capable of transferring power deeper into tissue than EMI and supports smaller RX sizes than EMI. A maximum spatial-peak-temporal-average intensity of 720 mW/cm^2 is imposed by the FDA for general tissue use [24]. This maximum safe limit is greater than the safe limit for EMI exposure. For these reasons, acoustic power transfer is investigated in this research.

Other technologies that could be used to power IMDs include energy harvesting and biological fuels cells. These technologies are under development and would currently only be feasible for extremely low power requirements. For further background, the reader is referred to wireless power transfer for IMD reviews found in [19], [20], [25].

1.3 Acoustic Transducer Types

There are various methods of converting electrical power to acoustic power and vice versa including electrostatic, piezoelectric, magnetostrictive, and electromagnetic.

The vast majority of publications make use of piezoelectric transducers because of the high coupling coefficient achieved by engineered materials such as PZT, and the commercial availability of piezoelectric elements. Within the realm of piezoelectric transducers, the two most common architectures used for acoustic applications are the plate and the diaphragm as shown in Figure 1-1. The plate vibrates in the bulk-mode in response to a sinusoidal voltage being applied to its electrodes. It is typically operated in the 3-3 direction (meaning electrical excitation is applied in the 3-direction to produce a mechanical response in the 3-direction and vice versa) to take advantage of the large coupling coefficient in that direction. The diaphragm vibrates in the flexure-mode in response to a sinusoidal voltage being applied to its electrodes. Its geometry constrains its operation to

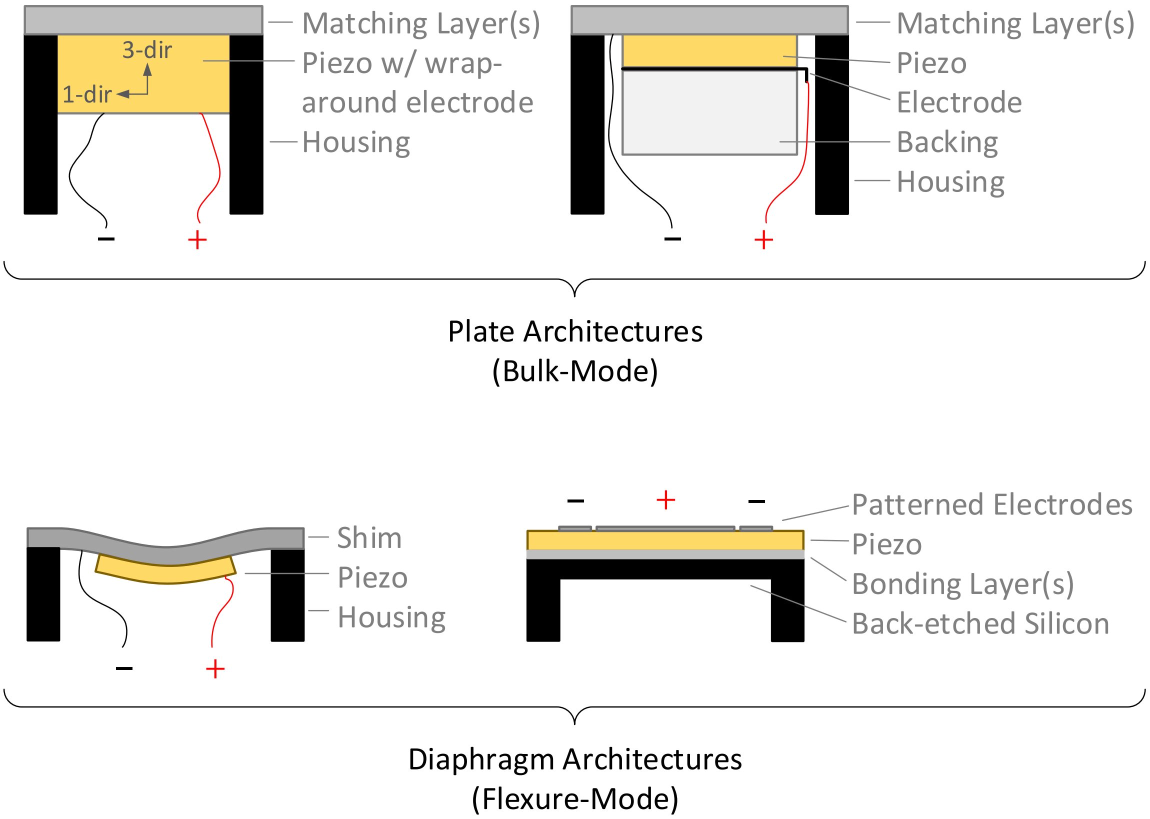

Figure 1-1. Piezoelectric plate and diaphragm architectures and examples of basic transducer schematics for each architecture.

utilize the 3-1 direction (meaning electrical excitation is applied in the 3-direction to produce a mechanical response in the 1-direction and vice versa). The vibration mode of each of these transducers results in vastly different frequencies and are thus the transducers are used for different applications. When comparing a plate and diaphragm of the same size, the plate operates at a much higher frequency than the diaphragm. The resonance frequency of the plate is determined by its thickness and the speed of sound of the piezoelectric material such that the plate's thickness is half of a wavelength in the piezo material at resonance. The resonance frequency of the diaphragm is determined by the compliance of the bending diaphragm structure. The thickness of the diaphragm is no thicker than 10% of its diameter (thicker structures result in the flexure vibration mode not being dominant), which results in a high compliance and low resonance frequency. The resonance frequency is further reduced when in contact with viscous fluids [26]. Traditionally, the plate is used in applications such as sonar, medical imaging, cleaning, and vaporization where the medium it is coupled to is water or tissue. These applications require a large power output and/or high frequencies. The diaphragm has been used in applications such as buzzers and speakers where the frequency range is in the audible spectrum (< 20 kHz) and the medium it is in contact with is air. In terms of IMDs, Table 1-1 gives an accounting of APT publications for IMD applications over the last 16 years. The table clearly shows that the vast majority of publications favor the plate as the architecture of choice. However, to power an IMD, the choice of which architecture to use depends on factors such as implant size and depth, whether acoustic data transmission is utilized [27], and allowable power sensitivity to disturbances in IMD position. The question of which architecture to use under what circumstance is the motivation of Chapter

Table 1-1. Accounting of piezoelectric transducer architectures, RX size, frequency, implant depth, and assumed medium used by APT for IMD publications over the last 16 years. Adapted from [19].

Year	Author, Ref	RX	TX	RX Diameter or L x W x H [mm]	Frequency [kHz]	Depth [mm]	Medium
2001	Kawanabe [28]	P	P	30	1000	7 to 100	Water, Goat
2002	Suzuki [29]	P	P	30 to 51	400 to 4000	7 to 100	Skin
2007	Arra [30]	P	P	25	840	5 to 105	Water
2007	Lee [31]	D	D	7	1.5	25	Pork
2009	Shigeta [32]	P	P	35	4200	70	Water
2010	Denisov [23]	P	P	2 to 10	≤ 1000	10 to 100	Tissue
2010	Mazzilli [33]	P	PF	6.3	1033	50	Water
2010	Ozeri [34]	P	P	15	673	40	Pork
2010	Shih [35]	D	D	7	35	60	Pork
2011	Larson [6]	P	P	1.13	1000	120	Rat hind limb
2011	Maleki [9]	P	P	5 x 1.02 x 1	2150	30	Tissue
2011	Shigeta [36]	P	P	44	1200	~32.3	Water
2012	Ozeri [37]	P	P	15	673	5 to 30	Pork
2012	Sanni [38]	P	P	10	200	≤ 70	Tissue
2013	Hori [39]	P	P	44	1200	50	Water
2013	Lee [40]	P	P	50	255	23	Pork
2013	Mo [41]	P	P	25	1000	0 to 400	Water
2013	Sanni [42]	P31	P31	10	200	80	Water, Oil
2013	Seo [43]	P	P	0.01 to 0.1	10000	2	Brain Tissue
2014	Chou [44]	P	P	4.4	200 to 400	25	Water, Oil, Pork
2014	He [45]	D	P	3.2 x 3.2 x 0.04	40	20 to 60	Water, Tissue
2014	Kim [10]	C	D	20 x 2 x 0.38	350	10 to 150	Pork
2014	Lee [46]	P	P	50	250	18 to 45	Pork
2014	Mazzilli [47]	PA	PA	1 x 5 x ???	1000	105	Water
2014	Ozeri [27]	P	P	15	765	150	Water
2014	Shahab [48]	P	S	6	47.7	20	Water
2014	Shmilovitz [49]	P	P	15	720	5 to 85	Water, Pork
2015	Charthad [50]	P	P	1 x 1 x 1.4 0.7 x 0.7 x 1	1000	30	Oil, Chicken
2015	Christensen [51]	P D	---	0.1 to 10	200 to 20000 30 to 2000	10 to 50	Muscle
2015	Fang [52]	P	PA	11.8	3250	100	Chicken, Pork
2015	Seo [53]	P	P	0.127 to 1 cubes	5000 to 10000	30	Water

Table 1-1 continued.

Year	Author, Ref	RX	TX	RX Diameter or L x W x H [mm]	Frequency [kHz]	Depth [mm]	Medium
2015	Song [54]	P	P	2 x 4 x 2 2 x 2 x 2 1 x 5 x 1	2300 2300 1150	200	Water
2015	Vihvelin [55]	P13	P13	8	1250 to 1350	5	Water, Pork
2015	Zhou [56]	P	P	8 x 16 x 2	672	67	Water
2016	Yu [4]	P	P	12.7	800	10 to 16	Water
2016	Charthad [57]	P	P	1.02 x 1.02 x 1.01	1000	60	Mineral Oil
2016	Guida [58]	P	P	9.5	700	50	Tissue Phantom
2016	Radziemski [59]	P	P	10 to 40	1000	3 to 50	Water, Pork, Beef
2016	Seo [60]	P	P	0.75 cube	1850	8.8	Tissue
2016	Weber [7]	P	PA	1.02 x 1.02 x 1.44	955	60	Mineral Oil
2017	Basaeri [61]	D	D	3.5 x 3.5 x 0.127	75	10	Water
2017	Meng [17]	P	P	1.2	1100	30	Castor Oil

P = Plate PA = Plate Array D = Diaphragm C = Cantilever
S = Sphere FP = Focused Plate P31 = 3-1 Plate

2. This chapter provides a comparison between the plate and diaphragm in terms of device size, implanted depth and power generation potential. As a rule of thumb, the diaphragm should be seriously considered for RX sizes in the submillimeter to low millimeter range. Other factors such as orientation and alignment also affect this decision and are discussed later in this chapter.

1.4 Modeling Techniques

The five most common methods used in published literature to model acoustic power transfer system (APTS) are: basic equations, circuit equivalent models (i.e., lumped element models), Huygens principle, and 2D and 3D finite elements/difference models.

1.4.1 Basic Equations

Basic acoustic equations are used as a high-level method of calculating a single specific feature of the APTS. The most common relationships referred to are the Rayleigh distance, reflection coefficient, matching layers, absorption, and beam divergence.

The depth at which to place the RX is often guided by the Rayleigh distance. The Rayleigh distance represents the distance away from the TX at which the near-field ends and the far-field starts. This distance is of particular note because it exhibits a high intensity region that is often described as a natural focus. Placing the RX farther into the far-field reduces the intensity on the RX face. Placing the RX into the near-field subjects the RX to high fluctuations in intensity as a function of depth. The Rayleigh distance is calculated in (1-1) where z_R is the Rayleigh distance, a_{TX} is the radius of the TX, and λ is the wavelength in the medium.

$$z_R = \left(\frac{a_{TX}^2}{\lambda} - \frac{\lambda}{4}\right) \approx \frac{a_{TX}^2}{\lambda} \tag{1-1}$$

The reflection coefficient is used to determine how much of the incident pressure is reflected away from the surface of the RX. For incident plane waves, the reflection coefficient is approximated by (1-2) [62] where R is the reflection coefficient, Z_1 is the acoustic impedance of the medium from which the pressure wave is coming (medium 1), Z_2 is the acoustic impedance of the medium to which the pressure wave is going (medium 2), θ_i is the angle of incidence of the pressure wave onto medium 2, θ_t is the angle of transmission of the pressure wave into medium 2. The acoustic impedance of a medium is typically approximated by multiplying the density and speed of sound of the medium. For piezoelectric transducers, the acoustic impedance depends on the electrical load connected to the transducer and can be approximated using transducer circuit equivalent models as discussed later in this chapter. It is important to note that the reflection coefficient calculation assumes incoming plane waves. In an APTS, this could be a fitting assumption for a RX that is placed well into the far-field where the waves appear approximately planar. However, when the RX is in the near field or near the Rayleigh distance, a realistic wave profile should be assumed. A realistic wave profile can be considered to be the superposition of spherically radiating pressure waves (meaning that each pressure wave appears approximately planar). Each of these waves strikes the RX at a different angle of incidence. The resulting reflection coefficient calculation would involve a distribution of incident and transmission angles. This is further discussed in Chapter 4. The pressure that is reflected away from the RX is found by multiplying the incident pressure by the reflection coefficient, R.

$$R = \frac{\dfrac{Z_2}{\cos(\theta_t)} - \dfrac{Z_1}{\cos(\theta_i)}}{\dfrac{Z_2}{\cos(\theta_t)} + \dfrac{Z_1}{\cos(\theta_i)}} \approx \frac{Z_2 - Z_1}{Z_2 + Z_1} \tag{1-2}$$

Calculation of the reflection coefficient leads to discussion of how to match the acoustic impedance of the TX and RX to the medium. Common practice is to employ a matching layer. A matching layer is a piece of material that is attached to the transmitting/receiving face of the TX or RX. It is theoretically most effective when it is a quarter-wavelength thick and has an acoustic impedance equal to (1-3) where Z_{ML} is the acoustic impedance of the matching layer. The wavelength in the matching layer is calculated as the speed of sound in the matching layer material divided by the operating frequency. This method assumes a single matching layer with no gluing layer or a gluing layer with negligible thickness compared to the matching layer thickness. When multiple matching layers are used or when the thickness of the gluing layers is significant, the method described in [63] can be employed. This method involves calculating a transfer matrix for each matching layer as given in (1-4) where T_n is the transfer matrix of the matching layer, t_n is the thickness of the matching layer, λ_n is the wavelength in the matching layer, and Z_n is the acoustic impedance of the matching. The transfer matrix of each matching layer is multiplied together to form a combined matching layer transfer matrix as given in (1-5). The components of the combine matrix are used in (1-6) to calculate the equivalent impedance of the transducer. In the equation, Z_{eq} is the equivalent impedance of the transducer and Z_P is the acoustic impedance of the piezo element. In the paper, the equivalent impedance is set equal to the acoustic impedance of the medium so that the optimal thicknesses of the matching layer can be determined (the gluing layer thickness is assumed fixed).

$$Z_{ML} = \sqrt{Z_1 Z_2} \tag{1-3}$$

$$T_n = \begin{bmatrix} \cos\left(\frac{2\pi t_n}{\lambda_n}\right) & jZ_n \sin\left(\frac{2\pi t_n}{\lambda_n}\right) \\ \frac{j}{Z_n}\sin\left(\frac{2\pi t_n}{\lambda_n}\right) & \cos\left(\frac{2\pi t_n}{\lambda_n}\right) \end{bmatrix} \tag{1-4}$$

$$[T] = T_1 T_2 \ldots = \begin{bmatrix} T_{11} & T_{12} \\ T_{21} & T_{22} \end{bmatrix} \tag{1-5}$$

$$Z_{eq} = \frac{T_{11} Z_P + T_{12}}{T_{21} Z_p + T_{22}} \tag{1-6}$$

Other forms of acoustic beam attenuation that are calculated using basic equations are absorption and beam divergence. Absorption is the conversion of acoustic power into heat and is calculate in (1-7) where α_0 is the absorption constant, n is the absorption exponent, f_{MHz} is the operating frequency in MHz, $\mathbb{P}_0$ is the initial acoustic power, and $\mathbb{P}_1$ is the acoustic power remaining after traveling a distance of z. Absorption is of particular concern to biological tissue because higher frequencies increase tissue heating and can lead to tissue damage and necrosis. As such, the United States FDA has imposed a maximum 7200 W/m^2 spatial-peak-temporal-average intensity limit for diagnostic ultrasound for general tissue use [24]. The intensity limit is lowered to 500 W/m^2 for ophthalmic applications. Beam divergence approximates the spreading of the acoustic beam in the far field. The beam divergence angle is given in (1-8) where ϕ_d is the divergence angle, a_{TX} is the radius of the TX, and λ is the wavelength in the medium. The beam divergence angle is measured relative to the propagation axis and is assumed to pass through the center of the TX as shown in Figure 1-2. The majority of the acoustic beam power lies between the propagation axis and the beam divergence angle. After calculating the beam divergence

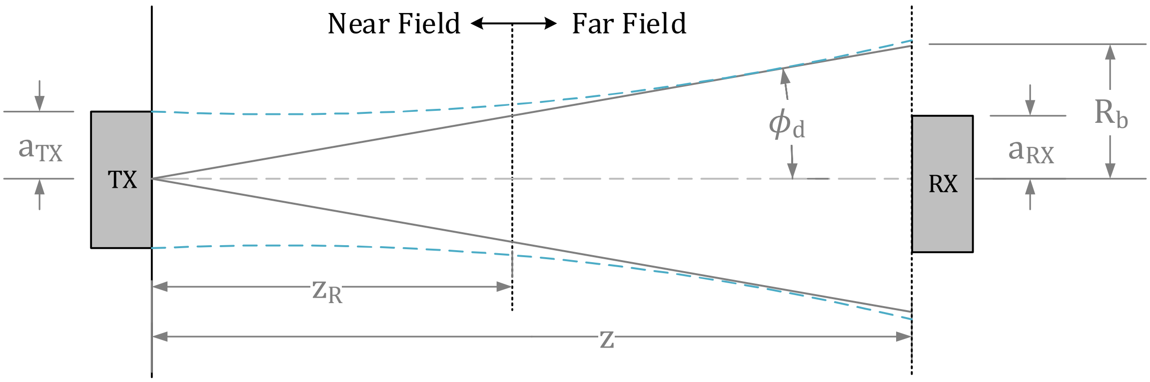

Figure 1-2. Diagram of beam divergence and Rayleigh distance calculation

angle, the beam radius is calculated as in (1-9) where z is the distance from the TX to the RX, and R_b is the beam radius. The power that reaches the RX is calculated in (1-10) where $\mathbb{P}_0$ is the initial acoustic power at the TX, $\mathbb{P}_1$ is the acoustic power remaining at the RX, and a_{RX} is the radius of the RX. It is important to note that the beam radius is calculated using the divergence angle only in the far-field. The beam radius is approximated as the TX radius when the RX is in the near-field.

$$\mathbb{P}_1 = \mathbb{P}_0 e^{-2\alpha_0 f_{MHz}^n z} \tag{1-7}$$

$$\phi_d \approx \sin^{-1}\left(\frac{0.61\lambda}{a_{TX}}\right) \tag{1-8}$$

$$R_b = z\tan(\phi_d) \tag{1-9}$$

$$\mathbb{P}_1 = \mathbb{P}_0 \frac{a_{RX}^2}{R_b^2} \tag{1-10}$$

1.4.2 Circuit Equivalent Models

Circuit equivalent models are used to model APTS because they have quick simulation times and can interface with a vast library of electrical components when simulated in a SPICE environment. These models are frequently used to design the driving circuitry of the TX, power conditioning circuitry of the RX, and signal conditioning circuitry of the IMD. Circuit elements are also used to model the mechanical or fluidic elements of the TX, medium, and RX. As such, they are capable of providing the acoustic impedance of a transducer as a function of transducer geometry and load impedance. For the plate architecture, the two most commonly used equivalent circuits for APT are the Mason model and the KLM model. These two circuit models are equivalent to each other [64] and are based on the 1D acoustic wave equations. The Mason model, shown in Figure 1-3, contains an electrical port and two mechanical ports. The electrical port is used to connect driving or receiving circuitry. One of the mechanical ports is used to interface with backing material and the other port is used to interface with matching layers or the medium. The piezo capacitance, C_0, is calculated in (1-11) where ϵ^T is the permittivity at zero stress, A_p is the cross-sectional area of piezo element, and t_P is the thickness of the piezo element.

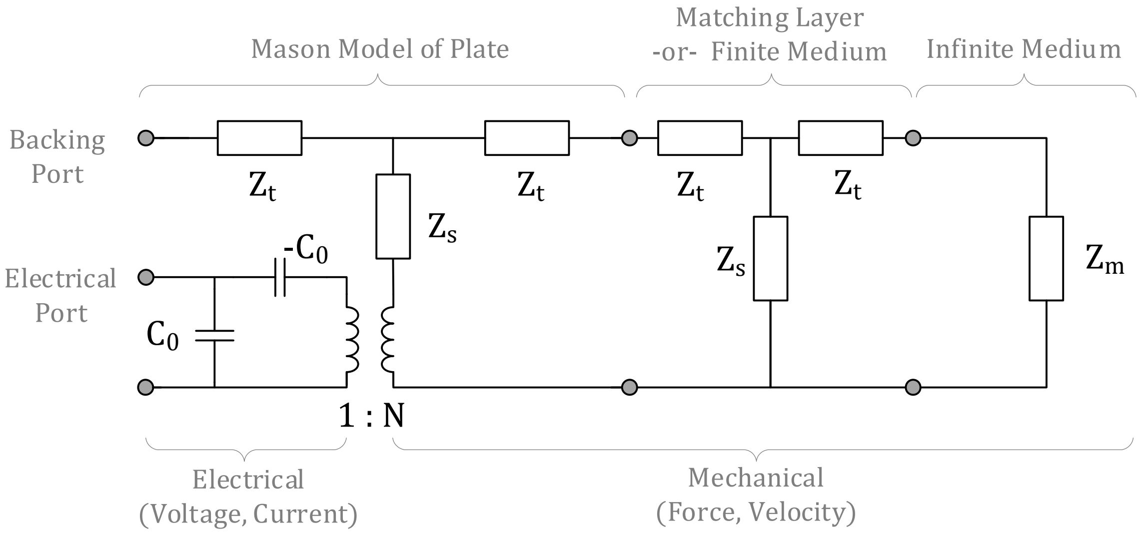

Figure 1-3. Mason equivalent circuit model for the piezoelectric plate (left). As an example, a matching layer equivalent circuit (center), which can also be used as a finite medium, and an infinite medium equivalent circuit (left) for a baffled piston radiator are attached.

The complex impedances Z_s and Z_t are given in (1-12) and (1-13) where ρ is the density of the material, c is the speed of sound in the material, A is the cross-sectional area of the material, f is the operating frequency, and t is the thickness of the material. The turns ratio, N, is given in (1-14) where k_{33} is the piezoelectric coupling coefficient in the 3-3 direction, and Y_3 is the modulus of elasticity in the 3-direction. The impedance of an infinite medium, Z_m, as seen by a circular piston in a rigid baffle, is given in (1-15) where k is the wavenumber (angular frequency divided by speed of sound), D is the diameter of the piston (the plate transducer), J_1 is the first order Bessel function, and H_1 is the first order Struve function. A useful tool for calculating the Struve function in Matlab is found in [65]. It should be noted that when connecting matching layer or medium equivalent circuits to the Mason model, the cross-sectional area of all circuit elements in the network must be the same. It is also useful to note that shorting a mechanical port of the Mason model to ground is physically equivalent to placing one side of the plate in contact with a vacuum. Other plate circuit equivalent models are available in RLC form [66]–[68], distributed parameter form [69], and experimentally driven form [70]. Each of these has a different level of abstraction such as single or multiple resonance frequencies, real or complex losses, and calculation of parameters from experimental data.

$$C_0 = \frac{\epsilon^T A_p}{t_p} \tag{1-11}$$

$$Z_s = -j\rho c A \csc\left(\frac{2\pi f t}{c}\right) \tag{1-12}$$

$$Z_t = j\rho c A \tan\left(\frac{\pi f t}{c}\right) \tag{1-13}$$

$$N = C_o k_{33} \sqrt{\frac{Y_3}{\epsilon^T}} \tag{1-14}$$

$$Z_m = \rho c A \left(1 - \frac{2J_1(kD)}{kD} - \frac{2H_1(kD)}{kD} j \right) \tag{1-15}$$

The diaphragm equivalent circuit model, shown in Figure 1-4, is derived using Kirchhoff's plate theory coupled with the piezoelectric equations. The figure shows that the diaphragm circuit has one electrical port and one fluidic port. The electrical source or load is attached to the electrical port and the medium is attached to the fluidic port. It is important to note that medium port of the plate and diaphragm circuit have different domains. The mechanical domain utilizes force and velocity as energy variables and the fluidic domain utilizes pressure and volumetric flow rate as energy variables. The volume displaced by the diaphragm structure when subjected to a pressure, P, and/or voltage, V, is given in (1-16) where $\Delta\mathbb{V}$ is the volume displaced, R_o is the outer radius of the diaphragm, r is the radius measured from the center of the diaphragm structure, and $w(r)$ is the

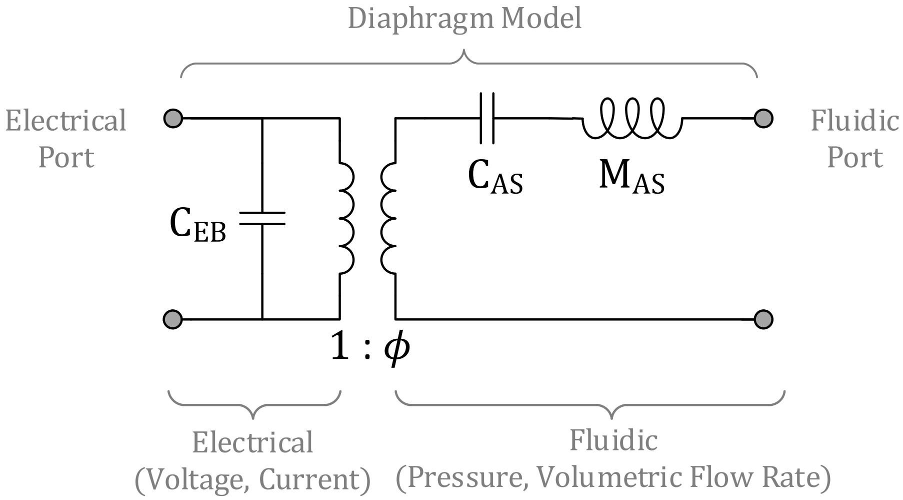

Figure 1-4. Piezoelectric diaphragm equivalent circuit.

transverse displacement of the diaphragm structure (i.e., displacement perpendicular to the diaphragm face) as a function of radius r. From the volume displacement, the fluidic compliance of the diaphragm, C_{AS}, is calculated from (1-17) where the $\Delta\mathbb{V}$ is calculated when pressure, P, is applied to the face of the diaphragm and voltage, V, is zero. The fluidic mass of the diaphragm, M_{AS}, is given in (1-18) where ρ_A is the areal density, and $w(r)$ and $\Delta\mathbb{V}$ are calculated when pressure, P, is applied and voltage, V, is zero. The blocked electrical capacitance, C_{EB}, is given in (1-19) where ϵ^T is the permittivity of the piezoelectric layer at zero stress, A_p is the area of the piezoelectric layer, t_p is the thickness of the piezoelectric layer, k_{31} is the piezoelectric coupling coefficient in the 3-1 direction. The effective piezoelectric coefficient, d_A, is given in (1-20) where $\Delta\mathbb{V}$ is calculated at an applied voltage, V, at zero applied pressure, P. The turns ratio, ϕ, is calculated in (1-21). Circuit element values can be calculated for a single-layer-shim partially-covered unimorph by referring to the relationships found in [71], [72]. For a partially-covered unimorph with an arbitrary number of shim layers, the working equations given in [73] can be used to calculate circuit element values (see Chapter 3 for errata details). The effect that fluid viscosity has on resonance frequency is discussed in Chapter 2.

$$\Delta\mathbb{V} = \int_0^{R_o} 2\pi r\, w(r)\, dr \tag{1-16}$$

$$C_{AS} = \frac{\Delta\mathbb{V}}{P} \quad at \quad V = 0 \tag{1-17}$$

$$M_{AS} = 2\pi\rho_A \int_0^{R_o} \left(\frac{w(r)}{\Delta\mathbb{V}}\right)^2 r\, dr \quad at \quad V = 0 \tag{1-18}$$

$$C_{EB} = \frac{\epsilon^T A_p}{t_p}(1 - k_{31}^2) \tag{1-19}$$

$$d_A = \frac{\Delta \mathbb{V}}{V} \quad at \quad P = 0 \tag{1-20}$$

$$\phi = -\frac{d_A}{C_{AS}} \tag{1-21}$$

1.4.3 Huygens Principle

Huygens principle is used to model either the pressure field emitted by the TX into the medium or the pressure distribution on the RX face as emitted by the TX. The idea behind Huygens principle is the superposition of acoustic waves to generate a realistic beam pattern. More specifically, the TX face is discretized into many small elements. Each of these elements is assumed to emit a spherically radiating pressure wave. The pressure and phase contribution of each spherical pressure wave at a specified point in the acoustic field is summed to determine the pressure at that point. The integration involved in summing the pressure contribution from each element on the TX face is expressed in the Rayleigh-Sommerfeld integral, (1-22) [62]. This expression is valid for any TX geometry. The corresponding diagram is given in Figure 1-5.

$$P = \frac{k\, Z\, u_0}{2\pi} \iint_{Source} \frac{\cos(\omega t - kr' + \pi/2)}{r'} \rho\, d\rho\, d\theta \tag{1-22}$$

1.4.4 Finite Element/Difference

Finite element and finite difference methods are used to simulate the full APTS in detail. Analysis is typically performed using the finite element method using commercial

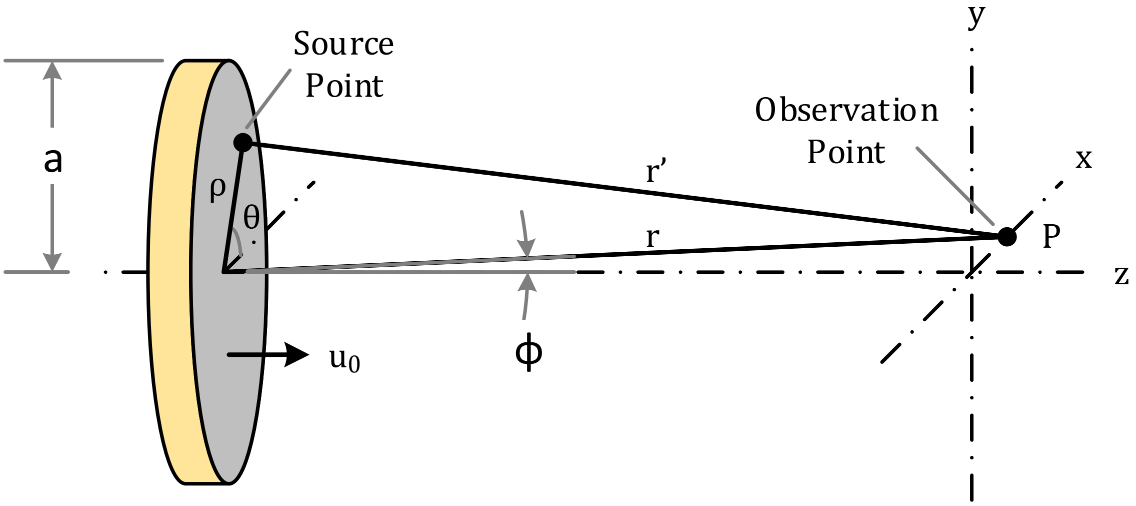

Figure 1-5. A diagram of integration variables involved in solving the Rayleigh Sommerfeld integral.

software such as COMSOL or ANSYS. In COMSOL, the Structural Mechanics Module is used to simulate the mechanical structure of the transducer. The MEMS Module is used to calculate lumped element parameters such as impedance and to interface with basic electronic components such as resistors, capacitors, inductors, and diodes. The Acoustics Module is used to simulate acoustic propagation and acoustic-structural interaction in the frequency and time domain. Of particular interest to APTS is the analysis of diameter, depth, orientation, alignment, frequency, and load as depicted in Figure 1-6. These parameters significantly affect the power delivered to the IMD. Diameter refers the diameter of the TX and RX, depth refers the axial separation distance between the TX and RX, orientation refers to rotation angle of the RX relative to the TX, alignment refers to the lateral offset of the RX relative to the TX, frequency is the operating frequency of the source (which is assumed to be at the resonance of the TX and RX unless otherwise stated), and load is electrical load attached to the RX transducer. Finite element analysis (FEA) provides the ability to analyze each of these parameters for a fully coupled APTS. The two

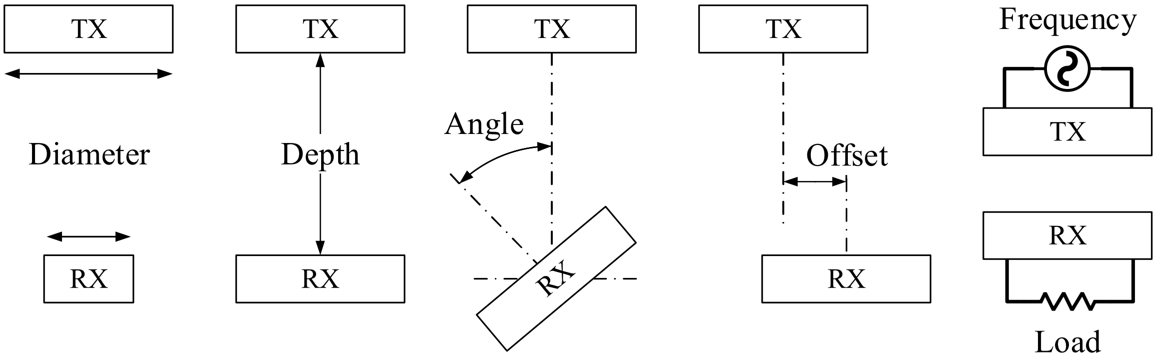

Figure 1-6. Significant parameters in an APTS: TX and RX diameter, depth, angle (orientation), offset (alignment), operating frequency, and electrical load.

types of FEA that are relevant for APTS analysis are 2D axisymmetric and 3D. 2D axisymmetric FEA is used to simulate an APTS with a TX and RX of differing diameter and arbitrary depth in a homogenous medium. 3D FEA can be used to simulate an inhomogeneous medium, arbitrary transducer shapes, and additionally account for RX orientation and alignment. 3D FEA clearly provides superior versatility, but is computationally intensive.

1.5 Synthesis

Each of the modeling techniques described above has advantages and disadvantages. Basic equations provide quick approximations and lend relational insight into the APTS. However, they are limited to specific transducer geometries, typically assume that acoustic wave profiles are planar, and generally apply to a single subsystem of the APTS at a time (e.g., pressure loss through the medium or reflection at the RX face). Circuit equivalent models provide quick and accurate simulations of electronics components and can approximate the entire APTS coupled with complicated driving, receiving, and conditioning circuitry. However, the APTS is limited to a one-dimensional (1D) representation that assumes plane waves. Huygens principle provides realistic beam pattern visualization for an arbitrary transducer shape. However, it does not account for reflections between the TX and RX and is unable to model inhomogeneous mediums. 2D axisymmetric FEA provides beam pattern visualization of realistic waves and can model the entire APTS system complete with basic electronics. However, the entire APTS system has to be axisymmetric, which limits its functionality to circular transducers that are unable to be laterally offset (misaligned) or rotated (misoriented) relative to each other. 3D FEA provides all the functionality that could ever be needed to model an APTS system including the ability to model RX depth, orientation, and alignment relative to the TX. However, it comes at the price of an expensive computation time. It should be noted that only circuit equivalent models and FEA models are able to estimate the end to end power transfer of the APTS.

Table 1-2 provides a list of the modeling techniques utilized in APTS for IMD publications over the last 16 years. Many of the design procedures used are a conglomeration of modeling techniques such as using basic equations or circuit models as a first order approximation then refining the design using 2D FEA. Some use 2D FEA to determine and optimize parameters for circuit models. Other methodologies rely solely on a single modeling technique. A special instance of circuit modeling is found in [48]. The paper derives analytical equations for a fully coupled system with a spherically radiating source, homogeneous medium, a cylindrical piezoelectric RX, and a load. Relationships are presented for a purely resistive optimal load, a resistive-inductive optimal load, and a resistive-capacitive optimal load. The paper provides useful relational insights into the

Table 1-2. Accounting of modeling techniques used by APT for IMD publications over the last 16 years. Adapted from [19].

Year	Author, Ref	Basic Equations	Circuit Equivalent	Huygens	2D FEA	3D FEA
2001	Kawanabe [28]					
2002	Suzuki [29]					
2007	Arra [30]	X				
2007	Lee [31]					
2009	Shigeta [32]					
2010	Denisov [23]		X			
2010	Mazzilli [33]	X	X			
2010	Ozeri [34]	X	X	X	X	
2010	Shih [35]	X				
2011	Larson [6]					
2011	Maleki [9]		X			
2011	Shigeta [36]		X		X	
2012	Ozeri [37]				X	
2012	Sanni [38]		EO			
2013	Hori [39]		X		X	
2013	Lee [40]	X		X		
2013	Mo [41]	X		X		FDTD
2013	Sanni [42]					
2013	Seo [43]	X	X			
2014	Chou [44]		X		X	
2014	He [45]				X	
2014	Kim [10]	X				
2014	Lee [46]	X		X		
2014	Mazzilli [47]	X	EO			
2014	Ozeri [27]	X	X			
2014	Shahab [48]		X*		X	
2014	Shmilovitz [49]	X	X			
2015	Charthad [50]		X			X
2015	Christensen [51]	X	X			
2015	Fang [52]					
2015	Seo [53]	X	X		X	
2015	Song [54]	X	X			
2015	Vihvelin [55]					
2015	Zhou [56]					
2016	Yu [4]		EO			
2016	Charthad [57]		X			
2016	Guida [58]					
2016	Radziemski [59]					
2016	Seo [60]					
2016	Weber [7]					
2017	Basaeri [61]				X	
2017	Meng [17]	X			X	

X = Used X* = Specialized Instance EO = Electronic Only FDTD = Finite Difference system of interest and other similar systems and accounts for beam divergence, but it does not have the capabilities to model orientation and alignment. Another procedure of note, [17], employs a 2D axisymmetric FEA in an iterative process to optimize the power transfer efficiency for a plate TX and RX. The method begins by applying diameter, thickness, and depth constraints to the RX then proceeds to loop through TX and RX diameters and thickness, using a brute force method, to maximize the power transfer efficiency. The method worked well for depth, diameter, frequency, and load optimization, but, as the author pointed out, was unable to account for orientation and alignment. Experimental results presented revealed that power transfer efficiency was cut in half at 1.5 mm misalignment.

The effect that orientation and alignment have on the voltage and power generated for an APTS appears to be generally acknowledged as shown in Table 1-3, but doesn't appear to be well understood. An observation of the table reveals that only one publication, [41], has addressed orientation and alignment in a simulation approach. This paper presents pressure on the RX face as a function of depth, orientation, and alignment for a fixed diameter. The information presented is difficult to decipher as many lines are plotted over each other and doesn't appear to account for load or describe the effect of frequency. All other papers that have addressed orientation and alignment have provided experimental data for their particular devices. The cause of this lack of modeling is most likely due to the difficulty of obtaining orientation and alignment data. From the description of modeling techniques above, Huygens principle appears to be a suitable candidate for obtaining this information because it can be used to estimate the pressure on the RX face emitted by the TX. However, further consideration reveals that reflections between the TX and RX are

Table 1-3. Accounting of significant APTS parameters examined in APT for IMD publications over the last 16 years. Both simulation and experimental parameters are listed. Parameters are listed if significant measurements or simulations were observed.

Year	Author, Ref	Load	Freq	Diameter	Depth	Offset	Angle
2001	Kawanabe [28]						
2002	Suzuki [29]				X		X
2007	Arra [30]				X	X	X
2007	Lee [31]	X	X				X
2009	Shigeta [32]	X	X		X		
2010	Denisov [23]			S	S		
2010	Mazzilli [33]						
2010	Ozeri [34]		X		S	X	
2010	Shih [35]		X				
2011	Larson [6]						X
2011	Maleki [9]				X		
2011	Shigeta [36]		S				
2012	Ozeri [37]					X	
2012	Sanni [38]		X				
2013	Hori [39]		XS		X	X	
2013	Lee [40]		X		X		X
2013	Mo [41]			S	S	S	S
2013	Sanni [42]		X		X		
2013	Seo [43]		S	S	S		
2014	Chou [44]				XS		
2014	He [45]	X	X		X	X	X
2014	Kim [10]				X	X	X
2014	Lee [46]		X		X		X
2014	Mazzilli [47]		X				
2014	Ozeri [27]	XS					
2014	Shahab [48]	S	S				
2014	Shmilovitz [49]		X			X	
2015	Charthad [50]	X	XS		X		
2015	Christensen [51]		XS	S	S		
2015	Fang [52]				X		
2015	Seo [53]		XS	XS			
2015	Song [54]						X
2015	Vihvelin [55]		X		X		
2015	Zhou [56]				X	X	
2016	Yu [4]				X	X	X
2016	Charthad [57]						
2016	Guida [58]						
2016	Radziemski [59]		X				
2016	Seo [60]		X		X	X	X
2016	Weber [7]						
2017	Basaeri [61]		XS				
2017	Meng [17]	XS	XS		XS	X	

X = Experimental Measurements S = Simulation Analysis Sweep / Optimization not accounted for in Huygens principle. These reflections contribute significantly to the power delivered to the IMD especially for IMDs that operate in the near-field or near the Rayleigh distance. A modeling technique that will model orientation and alignment effects is 3D FEA. However, this technique typically is avoided because of the steep computational cost. To put this simulation time in perspective, a sample 3D FEA simulation time for a single data point (a single value of depth, TX and RX diameter, frequency, load, orientation, and alignment) from Chapter 3 is 2777 seconds. Analyzing alignment with a sweep of 100 lateral offset data points for a fixed set of transducers at a fixed depth and frequency would take 3.21 days to complete assuming that no computational complications were experienced. Since the offset profile is a function of depth, as discussed in Chapter 4, multiple slices, each taking 3.21 days, would be required to understand the effects of alignment as a function of depth just for that particular set of transducers operating at that particular frequency. Since the offset profile is also a function of operating frequency and diameter, a massive amount of time would be spent on simulations to properly visualize the design space. This high computational cost provides the motivation for Chapters 3 and 4 of this dissertation.

Chapter 3 presents the development of a modeling technique that is able to model Depth, Orientation, and Alignment via Ray Tracing (DOART). This technique is a hybrid of circuit equivalent models, Huygens principle, and ray tracing. It is advantageous over 2D FEA because it can model the effects of orientation and alignment and the computation time is on the same order of magnitude. It is additionally advantageous over 3D FEA because it is at least one to two orders of magnitude faster. Table 1-4 gives a comparison of features for the five modeling techniques described above and DOART. As a trade-off

Table 1-4. Supported modeling features of the modeling techniques discussed. DOART is the modeling technique presented in this dissertation. Missing spaces indicate that modeling feature has not been observed.

Supported Modeling	Basic Eqns.	Circuit Equiv.	Huygens	2D FEA	3D FEA	DOART
Fully-Coupled APTS		X		X	X	X
TX & RX of differing diameter				X	X	X
Depth		X		X	X	X
Orientation					X	XX
Alignment					X	XX
Beam pattern visualization			XX	X	X	X
Inhomogeneous medium					XX	
Electronics interface		XX		X	X	X
Computation time	Low	Low	Mid	Mid	High	Mid
Wave type	Plane	Plane	Realistic	Realistic	Realistic	Realistic
Beam divergence	X		X	X	X	X
Absorption	X	X	X	X	X	X
Reflection	X	X		X	X	X
Matching Layers	X	X		X	X	X
Rayleigh distance	X		X	X	X	X
Circular transducers	X	X	X	X	X	X
Square transducers	X		X		X	E
Arbitrary planar shape transducers			X		X	E
Focused transducers	X		X	X	X	E
Phased arrays	X		X		X	E

X = Yes E = Extensible XX = Specialty feature of modeling technique to DOARTs speed, it doesn’t support inhomogeneous mediums. These types of mediums have not been considered in any of the publications presented in this dissertation, so this trade-off is assumed to be acceptable for the APT for IMD field of study. The table also shows that other features of DOART are extensible, such as different transducer geometries. The version of DOART presented in this dissertation supports circular transducers. The technique can be extended, without significant work, to include any planar transducer shape. Focused transducers would require more work.

Chapter 4 presents a nondimensional analysis of depth, orientation, and alignment. The effects of frequency, diameter, and load are also explored. In addition to the nondimensional analysis, the contribution of this chapter is a set of nondimensional graphs that are designed to aid IMD designers in determining IMD power sensitivity to depth, orientation, and alignment based on frequency and diameter selection. The simulation data for Chapter 4 are generated by the DOART modeling technique. In this work, DOART is implemented in a Matlab app with the current version requiring a minimum of Matlab R2017a to run. It should be noted however, that the modeling technique could be implemented in other programming languages such as Python. Dimensional and nondimensional design graphs can be generated for a specified set of TX and RX transducers using the app.

References

[1] M. R. Costanzo, L. W. Stevenson, P. B. Adamson, A. S. Desai, J. T. Heywood, R. C. Bourge, J. B. Ms, and W. T. Abraham, “Interventions linked to decreased heart failure hospitalizations during ambulatory pulmonary artery pressure monitoring,” *JACC Hear. Fail.*, 2016.

[2] P. B. Adamson, “CardioMEMS HF system clinical protocol example.” [Online].

Available: https://www.sjm.com/en/sjm/cardiomems.

[3] A. Guiseppi-Elie, S. Brahim, G. Slaughter, and K. Ward, “Design of a subcutaneous implantable biochip for monitoring of glucose and lactate,” *IEEE Sens. J.*, vol. 5, no. 3, pp. 345–355, 2005.

[4] H. Basaeri, D. Christensen, S. Roundy, Y. Yu, T. Nguyen, P. Tathireddy, and D. J. Young, “Ultrasonically powered hydrogel-based wireless implantable glucose sensor,” *2016 IEEE Sensors Proc.*, pp. 1–3, 2016.

[5] “Stanford engineer invents safe way to transfer energy to medical chips in the body.” [Online]. Available: http://news.stanford.edu/news/2014/may/electronic-wireless-transfer-051914.html. [Accessed: 18-May-2016].

[6] P. J. Larson and B. C. Towe, “Miniature ultrasonically powered wireless nerve cuff stimulator,” in *Neural Engineering (NER), 2011 5th Int. IEEE/EMBS Conf. on. IEEE*, 2011.

[7] M. J. Weber, A. Bhat, T. C. Chang, J. Charthad, and A. Arbabian, “A miniaturized ultrasonically powered programmable optogenetic implant stimulator system,” in *IEEE Topical Conf. on Biomed. Wireless Technologies, Networks, and Sensing*, 2016, pp. 12–14.

[8] A. Arbabian, T. C. Chang, M. L. Wang, J. Charthad, S. Baltsavias, M. Fallahpour, and M. J. Weber, “Sound technologies, sound bodies,” *IEEE Microwave Magazine*, no. December, pp. 39–54, 2016.

[9] T. Maleki, N. Cao, S. Hyun Song, C. Kao, S. Chu, A. Ko, and B. Ziaie, “An ultrasonically powered implantable micro-oxygen generator (IMOG),” *IEEE Trans. Biomed. Eng.*, vol. 58, no. 11, pp. 3104–3111, 2011.

[10] A. Kim, C. R. Powell, and B. Ziaie, “An implantable pressure sensing system with electromechanical interrogation scheme,” *IEEE Trans. Biomed. Eng.*, vol. 61, no. 7, pp. 2209–2217, 2014.

[11] M. A. Rothfuss, J. V Unadkat, M. L. Gimbel, M. H. Mickle, and E. Sejdic, “Totally implantable wireless ultrasonic doppler blood flowmeters : toward accurate miniaturized chronic monitors,” *Ultrasound Med. Biol.*, vol. 43, no. 3, pp. 561–578, 2017.

[12] P. R. Troyk, G. A. DeMichele, D. A. Kerns, and R. F. Weir, “IMES: An implantable myoelectric sensor,” *Annu. Int. Conf. IEEE Eng. Med. Biol. - Proc.*, pp. 1730–1733, 2007.

[13] K. D. Wise, D. J. Anderson, J. F. Hetke, D. R. Kipke, and K. Najafi, “Wireless implantable microsystems: High-density electronic interfaces to the nervous

system," *Proc. IEEE*, vol. 92, no. 1, pp. 76–97, 2004.

[14] Z. S. Zumsteg, C. Kemere, G. Driscoll, Stephen OSanthanam, R. E. Ahmed, K. V Shenoy, and T. H. Meng, "Power feasibility of implantable digital spike sorting circuits for neural prosthetic aystems," *IEEE Trans. Neural Syst. Rehabil. Eng.*, vol. 13, no. 3, pp. 272–279, 2005.

[15] E. Efeyini, "Healthcare sector outlook - how innovation could fuel growth," 2016. [Online]. Available: https://www.merrilledge.com/article/healthcare-innovation-investment-opportunities.

[16] Panasonic, "Energy solutions: a comprehensive guide to primary and rechargeable batteries." [Online]. Available: https://na.industrial.panasonic.com/sites/default/pidsa/files/downloads/files/battery-energy-catalog.pdf.

[17] M. Meng and M. Kiani, "Design and optimization of ultrasonic wireless power transmission links for millimeter-sized biomedical implants," *IEEE Trans. Biomed. Circuits Syst.*, vol. 11, no. 1, pp. 98–107, 2017.

[18] D. B. Shire, S. K. Kelly, J. Chen, P. Doyle, M. D. Gingerich, S. F. Cogan, W. A. Drohan, O. Mendoza, L. Theogarajan, J. L. Wyatt, and J. F. Rizzo, "Development and implantation of a minimally invasive wireless subretinal neurostimulator," *IEEE Trans. Biomed. Eng.*, vol. 56, no. 10, pp. 2502–2511, 2017.

[19] H. Basaeri, D. B. Christensen, and S. Roundy, "A review of acoustic power transfer for bio-medical implants," *Smart Mater. Struct.*, vol. 25, no. 12, pp. 1–23, 2016.

[20] K. Agarwal, R. Jegadeesan, Y. Guo, and N. V Thakor, "Wireless power transfer strategies for implantable bioelectronics : methodological review," *IEEE Rev. Biomed. Eng.*, vol. 10, no. c, pp. 1–28, 2017.

[21] R. F. J. Cleveland, D. M. Sylvar, and J. L. Ulcek, *Evaluating Compliance with FCC Guidelines for Human Exposure to Radiofrequency Electromagnetic Fields OET Bulletin 65*, no. August. 1997.

[22] I. C. on N.-I. R. Protection, "ICNIRP guidelines for limiting exposure to time-varying electric, magnetic and electromagnetic (up to 300 GHz)," *Health Phys.*, vol. 74, no. 4, pp. 494–522, 1998.

[23] A. Denisov and E. Yeatman, "Ultrasonic vs. inductive power delivery for miniature biomedical implants," in *Body Sensor Networks BSN 2010 International Conference on*, 2010, no. June, pp. 84–89.

[24] *Guidance for Industry and FDA Staff Information for Manufacturers Seeking Marketing Clearance of Diagnostic Ultrasound Systems and Transducers*. U.S.

Department of Health and Human Services, Food and Drug Administration, Center for Devices and Radiological Health, 2008.

[25] M. G. L. Roes, S. Member, J. L. Duarte, M. A. M. Hendrix, E. A. Lomonova, and S. Member, “Acoustic energy transfer : a review,” vol. 60, no. 1, pp. 242–248, 2013.

[26] M. Olfatnia, Z. Shen, J. M. Miao, L. S. Ong, T. Xu, and M. Ebrahimi, “Medium damping influences on the resonant frequency and quality factor of piezoelectric circular microdiaphragm sensors,” *J. Micromechanics Microengineering*, vol. 21, no. 4, p. 45002, Apr. 2011.

[27] S. Ozeri and D. Shmilovitz, “Simultaneous backward data transmission and power harvesting in an ultrasonic transcutaneous energy transfer link employing acoustically dependent electric impedance modulation,” *Ultrasonics*, vol. 54, no. 7, pp. 1929–1937, 2014.

[28] H. Kawanabe, T. Katane, H. Saotome, O. Saito, and K. Kobayashi, “Power and information transmission to implanted medical device using ultrasonic,” *Jpn. J. Appl. Phys.*, vol. 40, no. 5, pp. 3865–3866, 2001.

[29] S.-N. Suzuki, S. Kimura, T. Katane, H. Saotome, O. Saito, and K. Kobayashi, “Power and interactive information transmission to implanted medical device using ultrasonic,” *Japanese J. Appl. Physics, Part 1 Regul. Pap. Short Notes Rev. Pap.*, vol. 41, no. 5 B, pp. 3600–3603, 2002.

[30] S. Arra, J. Leskinen, J. Heikkilä, and J. Vanhala, “Ultrasonic power and data link for wireless implantable applications,” in *International Symposium on Wireless Pervasive Computing*, 2007, pp. 567–571.

[31] B.-S. Lee, P.-J. Shih, J.-J. He, W.-P. Shih, and W.-J. Wu, “A study of implantable power harvesting transducers,” in *The 14th International Symposium on: Smart Structures and Materials & Nondestructive Evaluation and Health Monitoring. International Society for Optics and Photonics*, 2007.

[32] Y. Shigeta, T. Yamamoto, K. Fujimori, M. Sanagi, S. Nogi, and T. Tsukagoshi, “Development of ultrasonic wireless power transmission system for implantable electronic devices,” in *Wireless Technology Conference, 2009. EuWIT 2009. European. IEEE*, 2009.

[33] F. Mazzilli, M. Peisino, R. Mitouassiwou, B. Cotte, P. Thoppay, C. Lafon, P. Favre, E. Meurville, and C. Dehollain, “In-vitro platform to study ultrasound as source for wireless energy transfer and communication for implanted medical devices.,” *Conf. Proc. IEEE Eng. Med. Biol. Soc.*, vol. 2010, pp. 3751–4, Jan. 2010.

[34] S. Ozeri and D. Shmilovitz, “Ultrasonic transcutaneous energy transfer for powering implanted devices.,” *Ultrasonics*, vol. 50, no. 6, pp. 556–66, May 2010.

[35] P.-J. Shih and W.-P. Shih, "Design, fabrication, and application of bio-implantable acoustic power transmission," *J. Microelectromechanical Syst.*, vol. 19, no. 3, pp. 494–502, Jun. 2010.

[36] Y. Shigeta, Y. Hori, K. Fujimori, K. Tsuruta, and S. Nogi, "Development of highly efficient transducer for wireless power transmission system by ultrasonic," in *2011 IEEE MTT-S International Microwave Workshop Series on Innovative Wireless Power Transmission: Technologies, Systems, and Applications*, 2011, pp. 171–174.

[37] S. Ozeri, B. Spivak, and D. Shmilovitz, "Non-invasive sensing of the electrical energy harvested by medical implants powered by an ultrasonic transcutaneous energy transfer link," *IEEE Int. Symp. Ind. Electron.*, pp. 1153–1157, 2012.

[38] A. Sanni, A. Vilches, and C. Toumazou, "Inductive and ultrasonic multi-tier interface for low-power, deeply implantable medical devices.," *IEEE Trans. Biomed. Circuits Syst.*, vol. 6, no. 4, pp. 297–308, Aug. 2012.

[39] Y. Hori, K. Fujimori, K. Tsuruta, and S. Nogi, "Design and development of highly efficient transducer for ultrasonic wireless power transmission system," *IEEJ Trans. Electron. Inf. Syst.*, vol. 132, no. 3, pp. 337–343, 2012.

[40] S. Q. Lee, W. Youm, and G. Hwang, "Biocompatible wireless power transferring based on ultrasonic resonance devices," *Proc. Meet. Acoust.*, vol. 19, pp. 1–9, 2013.

[41] C. Mo, S. Hudson, and L. J. Radziemski, "Effect of misalignment between ultrasound piezoelectric transducers on transcutaneous energy transfer," vol. 8688, no. 509, p. 868814, 2013.

[42] A. Sanni and A. Vilches, "Powering low-power implants using PZT transducer discs operated in the radial mode," *Smart Mater. Struct.*, vol. 22, no. 115005, 2013.

[43] D. Seo, J. M. Carmena, J. M. Rabaey, E. Alon, and M. M. Maharbiz, "Neural dust : an ultrasonic , low power solution for chronic brain-machine interfaces," arXiv:1307.2196 [q-bio.NC], July, 2013.

[44] T. C. Chou, R. Subramanian, J. Park, and P. P. Mercier, "A miniaturized ultrasonic power delivery system," *IEEE 2014 Biomed. Circuits Syst. Conf. BioCAS 2014 - Proc.*, pp. 440–443, 2014.

[45] Q. He, J. Liu, B. Yang, X. Wang, X. Chen, and C. Yang, "MEMS-based ultrasonic transducer as the receiver for wireless power supply of the implantable microdevices," *Sensors Actuators, A Phys.*, vol. 219, pp. 65–72, 2014.

[46] S. Q. Lee, W. Youm, G. Hwang, K. S. Moon, and Y. Ozturk, "Resonant ultrasonic wireless power transmission for bio-implants," vol. 9057, p. 90570J, 2014.

[47] F. Mazzilli, E. G. Kilinc, and C. Dehollain, “3.2 mW ultrasonic LSK modulator for uplink communication in deep implanted medical devices,” *IEEE 2014 Biomed. Circuits Syst. Conf. BioCAS 2014 - Proc.*, pp. 636–639, 2014.

[48] S. Shahab and a Erturk, “Contactless ultrasonic energy transfer for wireless systems: acoustic-piezoelectric structure interaction modeling and performance enhancement,” *Smart Mater. Struct.*, vol. 23, no. 12, p. 125032, 2014.

[49] D. Shmilovitz, S. Ozeri, C. C. Wang, and B. Spivak, “Noninvasive control of the power transferred to an implanted device by an ultrasonic transcutaneous energy transfer link.,” *IEEE Trans. Biomed. Eng.*, vol. 61, no. 4, pp. 995–1004, 2014.

[50] J. Charthad, M. J. Weber, T. C. Chang, and A. Arbabian, “A mm-sized implantable medical device (IMD) with ultrasonic power transfer and a hybrid bi-directional data link,” *IEEE J. Solid-State Circuits*, vol. 50, no. 8, pp. 1741–1753, 2015.

[51] D. B. Christensen and S. Roundy, “Ultrasonically powered piezoelectric generators for bio-implantable sensors: Plate versus diaphragm,” *J. Intell. Mater. Syst. Struct.*, pp. 1–14, 2015.

[52] B. Fang, T. Feng, M. Zhang, and S. Chakrabartty, “Feasibility of B-mode diagnostic ultrasonic energy transfer and telemetry to a cm2 sized deep-tissue implant,” *Proc. - IEEE Int. Symp. Circuits Syst.*, vol. 2015–July, pp. 782–785, 2015.

[53] D. Seo, J. M. Carmena, J. M. Rabaey, M. M. Maharbiz, and E. Alon, “Model validation of untethered, ultrasonic neural dust motes for cortical recording,” *J. Neurosci. Methods*, vol. 244, pp. 114–122, 2015.

[54] S. H. Song, A. Kim, and B. Ziaie, “Omni-directional ultrasonic powering for mm-scale implantable biomedical devices,” *Biomed. Eng. IEEE Trans.*, vol. 62, no. 11, pp. 2717–2723, 2015.

[55] H. Vihvelin, J. Leadbetter, M. Bance, J. A. Brown, and R. B. A. Adamson, “Compensating for tissue changes in an ultrasonic power link for implanted medical devices,” *IEEE Trans. Biomed. Circuits Syst.*, no. April, 2015.

[56] J. Zhou, A. Kim, and B. Ziaie, “An ultrasonically controlled power management system for implantable biomedical devices,” *Biomed. Circuits Syst. …*, pp. 1–4, 2015.

[57] J. Charthad, S. Baltsavias, D. Samanta, T. C. Chang, M. J. Weber, N. Hosseini-nassab, R. N. Zare, and A. Arbabian, “An ultrasonically powered implantable device for targeted drug delivery,” in *IEEE Engineering in Medicine and Biology Society*, 2016, pp. 541–544.

[58] R. Guida, G. E. Santagati, and T. Melodia, “A 700 kHz ultrasonic link for wireless

powering of implantable medical devices," in *IEEE Sensors*, 2016, pp. 0–2.

[59] L. Radziemski and I. R. S. Makin, "In vivo demonstration of ultrasound power delivery to charge implanted medical devices via acute and survival porcine studies," *Ultrasonics*, vol. 64, pp. 1–9, 2016.

[60] D. Seo, R. M. Neely, K. Shen, J. M. Rabaey, J. M. Carmena, M. M. Maharbiz, U. Singhal, and E. Alon, "Wireless recording in the peripheral nervous system with ultrasonic neural dust neuron neuroresource wireless recording in the peripheral nervous system with ultrasonic neural dust," *Neuron*, vol. 91, no. 3, pp. 1–11, 2016.

[61] H. Basaeri and S. Roundy, "A micromachined ultrasonic power receiver for biomedical implants," in *Proceedings of SPIE*, 2017, vol. 10164, pp. 1–7.

[62] D. A. Christensen, *Ultrasonic Bioinstrumentation*. John Wiley & Sons, Ltd, 1988.

[63] D. Callens, C. Bruneel, and J. Assaad, "Matching ultrasonic transducer using two matching layers where one of them is glue," *NDT E Int.*, vol. 37, no. 8, pp. 591–596, Dec. 2004.

[64] S. Sherrit, S. P. Leary, B. P. Dolgin, and Y. Bar-Cohen, "Comparison of the Mason and KLM equivalent circuits for piezoelectric resonators in the thickness mode," in *1999 IEEE Ultrasonics Symposium. Proceedings. International Symposium (Cat. No.99CH37027)*, 1999, vol. 2, pp. 921–926.

[65] Theo2, "Struve functions," *Matlab File Exchange*, 2012. [Online]. Available: https://www.mathworks.com/matlabcentral/fileexchange/37302-struve-functions?s_tid=srchtitle.

[66] M. Guan and W.-H. Liao, "Studies on the circuit models of piezoelectric ceramics," *Int. Conf. Inf. Acquis. 2004. Proceedings.*, pp. 26–31, 2004.

[67] W. P. Mason, "An electromechanical representation of a piezoelectric crystal used as a transducer," *Proc. Inst. Radio Eng.*, vol. 23, no. 10, pp. 1252–1263, 1935.

[68] H. A. C. Tilmans, "Equivalent circuit representation of electromechanical transducers: I. Lumped-parameter systems," *J. Micromechanics Microengineering*, vol. 6, no. 1, pp. 157–176, 1996.

[69] H. A. C. Tilmans, "Equivalent circuit representation of electromechanical transducers : II . Distributed-parameter systems," *J. Micromechanics Microengineering*, vol. 7, no. 4, pp. 285–309, 1997.

[70] J. Kim, B. L. Grisso, J. K. Kim, D. S. Ha, D. J. Inman, and A. U. P. Ceramics, "Electrical modeling of piezoelectric ceramics for analysis and evaluation of sensory systems," in *SAS 2008 - IEEE Sensors Applications Symposium*, 2008, pp. 122–127.

[71] S. A. N. Prasad, Q. Gallas, S. B. Horowitz, B. D. Homeijer, B. V. Sankar, L. N. Cattafesta, and M. Sheplak, “Analytical electroacoustic model of a piezoelectric composite circular plate,” *AIAA J.*, vol. 44, no. 10, pp. 2311–2318, Oct. 2006.

[72] S. A. N. Prasad, “Two-port electroacoustic model of a piezoelectric composite circular plate,” University of Florida, 2002.

[73] M. Deshpande and L. Saggere, “An analytical model and working equations for static deflections of a circular multi-layered diaphragm-type piezoelectric actuator,” *Sensors and Actuators*, vol. 136, pp. 673–689, 2007.

CHAPTER 2

ULTRASONCALLY POWERED PIEZOELECTRIC GENERATORS FOR BIO-IMPLANTABLE SENSORS: PLATE VERSUS DIAPHRAGM

The final, definitive version of this paper has been published in volume 27, issue 8, in May 2015 by SAGE Publications Ltd. All rights reserved. © David Brent Christensen & Shad Roundy. The article can be found at http://journals.sagepub.com/doi/abs/10.1177/1045389X15585897

CHAPTER 3

A COMPUTATIONALLY EFFICIENT TECHNIQUE TO MODEL DEPTH, ORIENTATION AND ALIGNMENT VIA RAY TRACING IN ACOUSTIC POWER TRANSFER SYSTEMS

This chapter was submitted to Smart Materials and Structures journal managed by Institute of Physics Publishing on June 27, 2017. The published version of this chapter has been published in volume 26, number 12, in Nov 2017 by IOP Publishing. The article can be found at https://doi.org/10.1088/1361-665X/aa95af.

CHAPTER 4

NONDIMENSIONAL ANALYSIS OF DEPTH, ORIENTATION, AND ALIGNMENT IN ACOUSTIC POWER TRANSFER SYSTEMS

This chapter was submitted to Smart Materials and Structures journal managed by Institute of Physics Publishing on July 21, 2017 and is under review.

4.1 Abstract

Acoustic power transfer systems are typically comprised of an electrical source, acoustic transmitter (TX), medium through which the acoustic waves propagate, acoustic receiver (RX) and an electrical load. The voltage and power delivered to the load from the TX is a function of RX position (depth, orientation, and alignment relative to the TX), frequency, TX and RX diameter, and source and load impedance. In applications where the RX position is not fixed, such as in implantable medical devices, slight disturbances in RX position can result in a severe reduction in voltage and power delivered to the load. Therefore, the sensitivity of voltage and power delivered to the load as a function of RX position is crucial to system design. This paper presents an analysis of the voltage and power delivered to the load as a function of RX depth, orientation, alignment, frequency, RX and TX diameter, and load impedance. Design graphs are developed and presented as a means of visualizing the sensitivity of voltage and power to system parameters. Nondimensional design graphs are then generated to broaden the applicability of simulation results.

4.2 Introduction

Acoustic power transfer systems have gained interest in the past decade because of their application to implantable medical devices. Implantable medical devices are devices that are implanted into biological tissue to perform a diagnostic or therapeutic function. A recent review of acoustic power transfer for implantable medical devices can be found in [1]. Acoustic power transfer systems, as commonly defined in literature, are comprised of an electrical source, acoustic transmitter (TX), medium (e.g., tissue or water) through which acoustic waves propagate, acoustic receiver (RX), and electrical load. The electrical source powers the TX, which is typically piezoelectric. The TX is in contact with and emits acoustic waves into the medium to the RX which is implanted in the medium. The RX, which is typically piezoelectric, transduces the acoustic power into electrical power utilized by the electrical load (for example, a glucose sensor). For a fixed medium, the voltage and power delivered to the electrical load are dependent on the following system parameters: load impedance, operating frequency, RX position relative to the TX, and TX and RX diameter. For transducers that have a circular cross-section, the RX position relative to the TX can be defined using three parameters: depth, angle, and offset. Depth is the axial distance between the TX and RX. Angle, also referred to as orientation, is the angle between the RX face and the TX face (i.e., angle is equal to zero when the TX and RX faces are parallel to each other). Offset, also referred to as alignment, is the lateral distance between the center of the TX and center of the RX. Depth, angle, and offset are defined graphically in Figure 4-1.

The majority of published research papers addressing acoustic power transfer for implantable medical devices address, to some extent, voltage and/or power delivered to the load as a function of depth [2]–[25]. Papers addressing voltage and/or power delivered

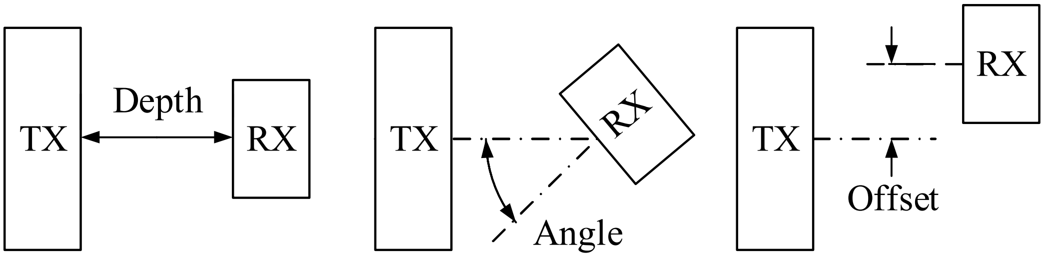

Figure 4-1. Diagram of depth, angle (orientation), and offset (alignment) degrees of freedom.

to the load as a function of offset and angle are fewer in number and can be found in [4], [5], [8], [11], [12], [15], [16], [21], [22], [26]. These papers consider orientation and alignment in a narrow scope: offering experimental and/or simulation data for a particular device. This information is useful for the particular device being analyzed, but offers limited insight into other acoustic power transfer systems. [12] provides dimensional simulation analysis on alignment and orientation using a finite difference time domain model for a specific device, but the analysis does not provide details about the effect that frequency, TX and RX diameter, and load impedance have on voltage and power delivered to the load. To the authors' knowledge, an analysis of voltage and power delivered to the load as a function of load impedance, operating frequency, depth, orientation, alignment, and TX and RX diameter has not been previously published. The purpose of this paper is to provide such an analysis. To accomplish this purpose, simulation data is analyzed dimensionally and compiled into design graphs to provide insight into voltage and power sensitivity to system parameters. Nondimensional design graphs are then generated to broaden the applicability of the data. This paper presents the following: 1) Modeling technique, system parameters and simulation assumptions. 2) Optimal load as a function of depth. 3) Voltage and power as a function of depth, and the depth magnitude and fluctuation design graphs. 4) Voltage and power as a function of angle, and the half angle design graph. 5) Voltage and power as a function of offset, and the half offset design graph. 6) Application of design graph data to scaled versions of the acoustic power transfer system using nondimensional parameters.

4.3 System Parameters and Assumptions

A diagram of the acoustic power transfer system of interest is given in Figure 4-2. The TX and RX are circular bulk-mode piezoelectric transducers with air backing and titanium matching layer. The use of an air backing increases the quality factor of the transducers and thus increases the power emitted by the TX and received by the RX at resonance. Titanium is chosen as the matching layer because it is a biocompatible material that is commonly used in medical applications. Material properties of the assumed piezoelectric material and titanium matching layer are given in Table 4-1. To model this system efficiently, the modeling technique described in Chapter 3 is used to obtain simulation data. All simulation data assume that the TX and RX have the same resonance frequency and that the TX is operating at resonance. At resonance, the impedance of the TX and RX is typically a minimum. TX and RX impedance affects the reflection coefficient

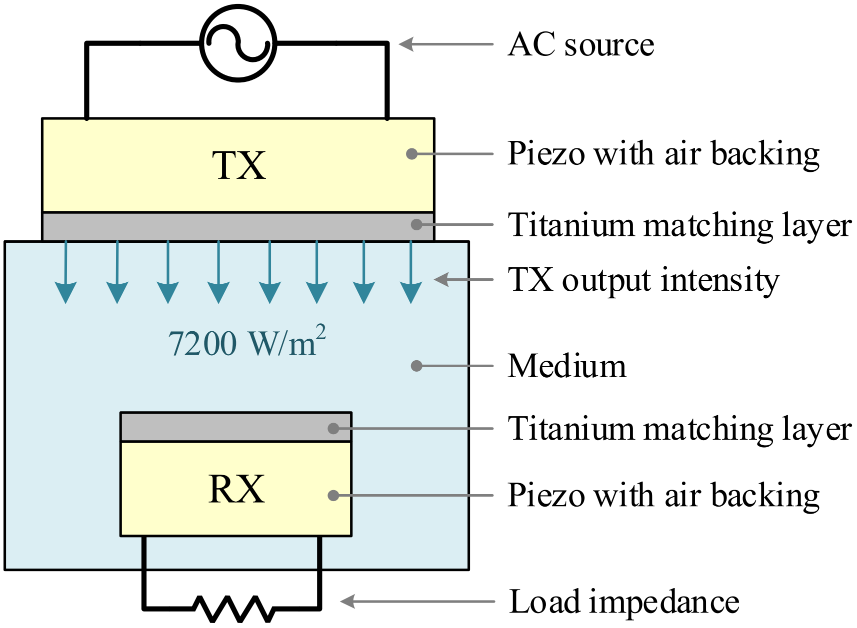

Figure 4-2. System diagram comprised of a source, TX, medium, RX, and load. The TX and RX have titanium matching layers and the TX emits an acoustic intensity of 7200 W/m^2.

Table 4-1. Material properties of the TX and RX piezo elements and titanium matching layer.

Material Property	Units	Value
Piezo Element		
Density	kg/m^3	7600
Speed of Sound	m/s	4025
Young's Modulus (3-dir)	GPa	54
Relative Permittivity	–	1950
Piezo Coupling Coeff. (3-3 dir)	–	0.46
Dielectric Loss (Loss Tangent)	%	1.5
Mechanical Quality Factor	–	80
Titanium Matching Layer		
Density	kg/m^3	4500
Speed of Sound	m/s	4916
Young's Modulus	GPa	115

at the TX and RX face, and thus affects the power that passes into the RX and the magnitude of reflections bouncing back and forth between the TX and RX. The TX outputs a continuous-wave acoustic intensity of 7200 W/m^2, which is the spatial-peak-temporal-average intensity limit in the human body for diagnostic ultrasound applications [27]. This intensity is used to provide an idea of achievable voltage and power levels in the dimensional graphs presented. The medium is considered to be homogeneous with an assigned absorption coefficient and absorption frequency exponent to account for absorption of acoustic waves through the medium. The apparent medium viscosity affects the quality factor of the transducer as described in [20]. Assumed material properties of the medium are meant to approximate lossy tissue, such as muscle, and are given in Table 4-2 [28][20].

Table 4-2. Material properties of the medium.

Medium Properties	Units	Value
Density	$\mathrm{kg/m^3}$	1070
Speed of Sound	$\mathrm{m/s}$	1566
Absorption Coefficient	$\mathrm{Np/m \cdot MHz}$	15
Absorption Freq. Exponent	$-$	1
Kinematic Viscosity	$\mathrm{m^2/s}$	0.15

4.4 Load

The first parameter of interest is the RX load because the optimal load resistance must be calculated (or an arbitrary load specified) before conducting further simulations. The optimal load in this paper is found by simulating the entire system to calculate load power as a function of real load impedance. The optimal load impedance is chosen as the real impedance at which maximum power is delivered to the load. It is useful to note that although complex impedance matching increases the voltage and power delivered to the load, implant device size restrictions may render it impractical to fit the required inductor in the device. With this assumption, the voltage and power levels in this paper represent a lower limit of theoretically achievable values. Many acoustic power transfer systems found in literature assume a fixed load for a fixed frequency. This is a practical assumption. However, it should be noted that optimal load fluctuates slightly as a function of depth as shown in Figure 4-3. This is due to the formation of acoustic standing waves in the medium between the TX and RX. As the depth between the TX and RX changes, the load sees the construction and destruction of these standing waves as a change in system impedance. To maintain optimal power to the load, the load impedance must change to match the fluctuating system impedance. In the figure, a 10-mm-diameter TX and RX operating at

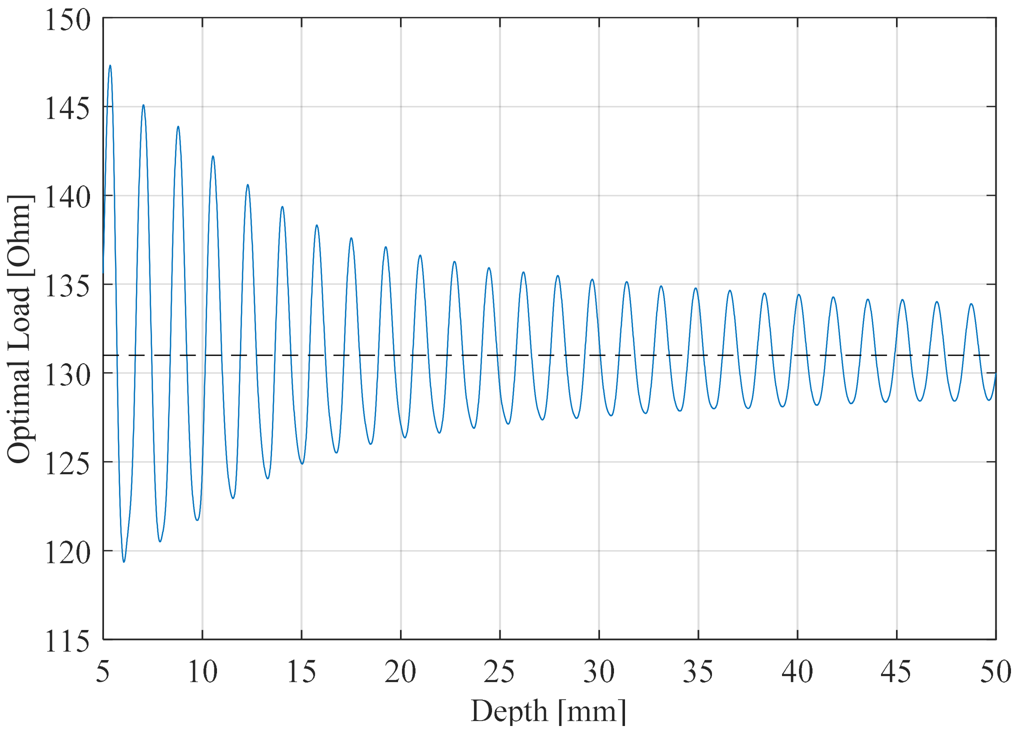

Figure 4-3. Optimal load impedance as a function of depth (blue line) for a 10-mm-diameter TX and RX operating at 450 kHz. Fixed-average optimal load impedance shown as black dotted line.

450 kHz are used. Greater optimal load fluctuation occurs closer to and in the near-field region, which is at 6.67 mm. To illustrate the voltage and power variation associated with this fluctuation in load, the voltage and power at the fixed-average optimal load, 131 ohms, is compared to the voltage and power at the actual optimal load in Figure 4-4. The voltage varies on average ±1.35% and the power varies on average -0.03%. For the remainder of this paper, all references to optimal load refer to the fixed-average optimal load.

4.5 Depth

The second parameter of interest is depth. As the axial distance between the TX and RX changes, the load voltage and power fluctuate as a result of acoustic standing waves

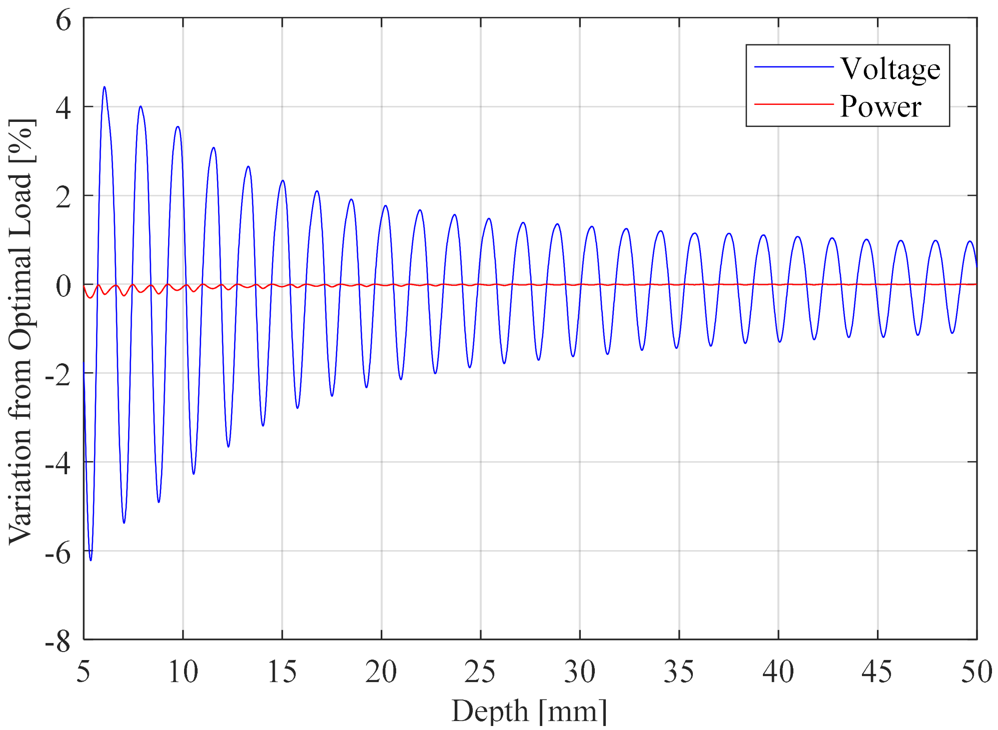

Figure 4-4. Variation in voltage and power caused by assuming a fixed-average optimal load impedance instead of a depth-dependent optimal load impedance for a 10-mm-diameter TX and RX operating at 450 kHz.

reflecting back and forth between the TX and RX. In graphical form, this data is difficult to interpret when comparing with other such similar data as shown in Figure 4-5. Inspection of the data reveals that it can be interpreted as the superposition of two signals. The first signal is the large signal, or DC signal, that represents the mean value of the RMS voltage or average power as a function of depth. The second signal is the small signal, or AC signal, that represents the sinusoidal fluctuation in the RMS voltage or average power and is a result of standing waves. The distance between standing wave peaks, as seen by the load, is given in (4-1) where $\Delta\mathbb{z}$ is the change in depth required for the load voltage or power to encounter the next spatial resonance peak, c is the speed of sound in the medium, f is the operating frequency, and λ is the wavelength in the medium. Figure 4-6 gives a graphical

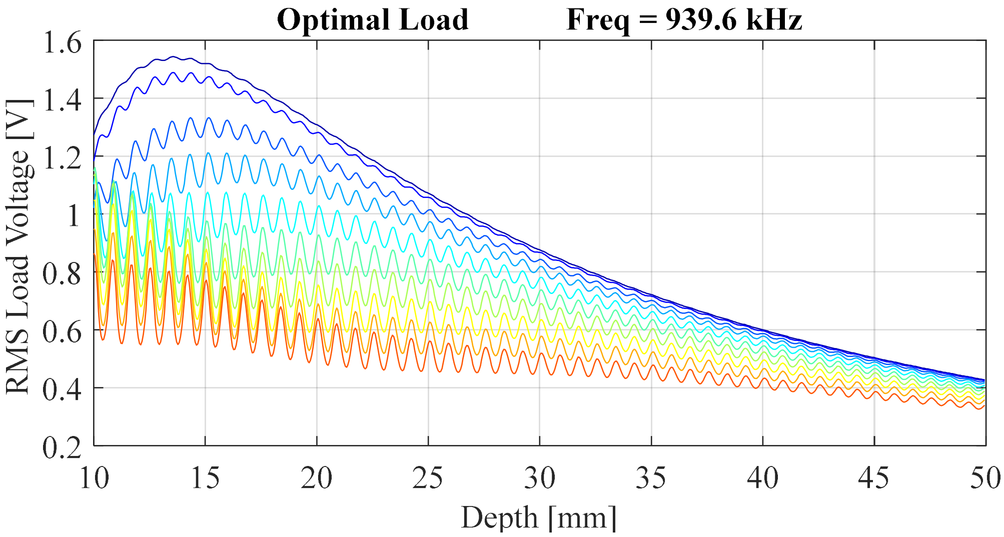

Figure 4-5. Load voltage as a function of depth for a 10-mm diameter TX operating at 939.6 kHz. This is the original simulation data before being split into mean (DC) and fluctuation (AC) components. Each line represents a RX diameter from 1 mm (dark blue) to 10 mm (red).

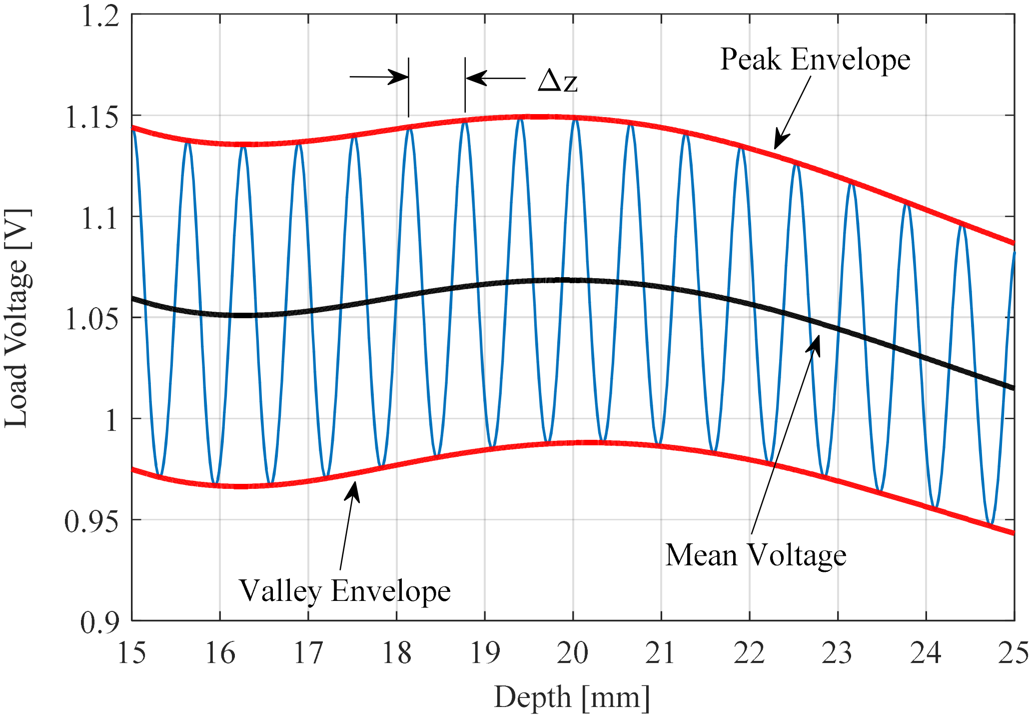

Figure 4-6. Decomposition of load voltage into a mean value and a fluctuation value. The fluctuation voltage is defined as the difference between the peak and valley envelopes. The mean voltage is defined as the mean of the peak and valley envelopes.

example of how mean and fluctuation values of voltage are calculated. In the figure, voltage fluctuation is the difference between the peak and valley envelopes and the mean voltage is the mean of the peak and valley envelopes. Depth data are collected when angle and offset are equal to zero.

$$\Delta\mathbb{z} = \frac{c}{2f} = \frac{\lambda}{2} \tag{4-1}$$

The first design graph is the depth magnitude design graph and is demonstrated in Figure 4-7. The depth magnitude design graph gives the mean voltage and power as a function of depth. In other words, it gives the DC signal of the depth data. Each line represents a RX diameter from 1 mm (dark blue) to 10 mm (red). The data show that voltage and power generally decrease with an increase in depth. This signal attenuation is a result of beam divergence and absorption in the medium. It is notable that the voltage is smaller for larger RX diameters, particularly near the Rayleigh distance. At the Rayleigh distance, 14.58 mm in this case, a maximum voltage is generated for smaller RX diameters. This is due to the nature of the acoustic beam emitted from the TX as shown in Figure 4-8. An inspection of the figure reveals that the beam is more intense near the propagation axis and exhibits a high intensity region around the Rayleigh distance. The intensity profile in the figure is generated for a 10-mm-diameter TX operating at 939.6 kHz using the formulation described in [29] and evaluated using Gauss quadrature. A small RX placed in the high intensity region sees a high intensity on its entire face and generates a high voltage. A large RX placed in the high intensity region sees a high intensity at the center of its face and a low intensity on the edges of its face. This results in a lower average intensity on the RX face and thus a lower generated voltage. Also of note is that voltage and power for the 10-mm diameter RX (red line) continually increase with a decrease in depth. This is the

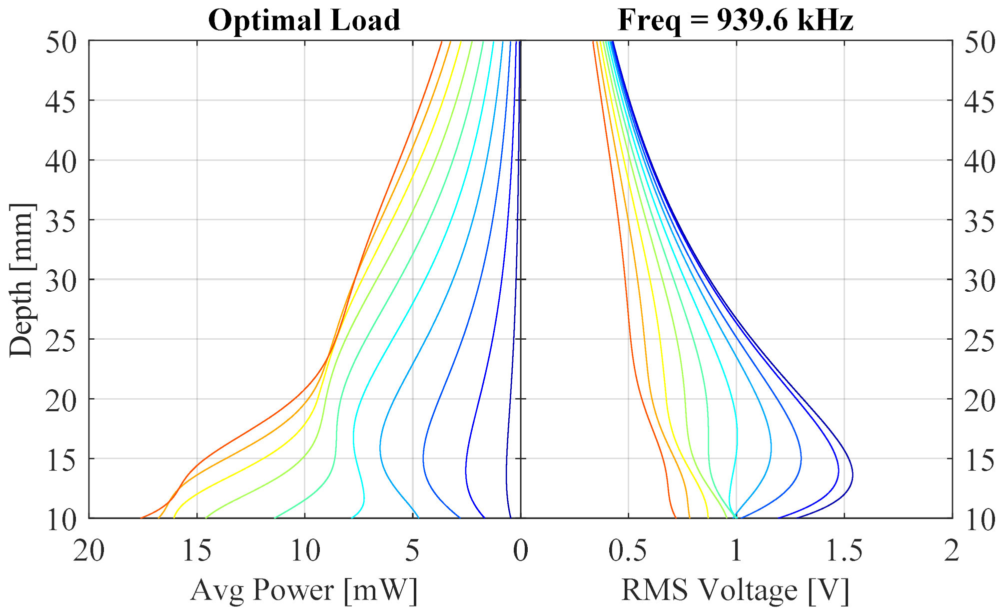

Figure 4-7. Depth magnitude design graph. Mean voltage and power as a function of depth for a TX and RX operating at 939.6 kHz with a fixed-average optimal load as described in the Load section of this paper. Each line represents a RX diameter from 1 mm (dark blue) to 10 mm (red).

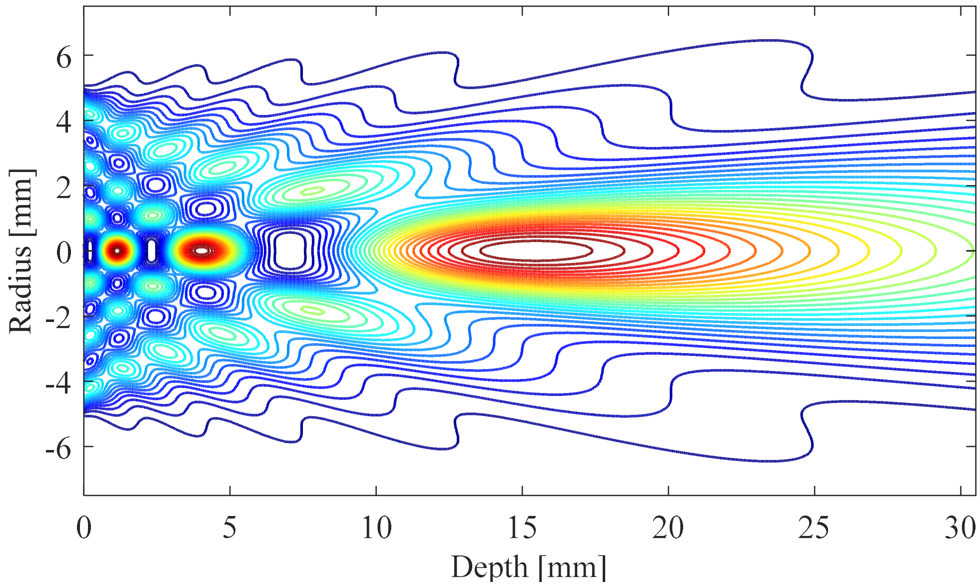

Figure 4-8. Contour plot of acoustic intensity emitted from a 10-mm-diameter TX operating at 939.6 kHz. The radius axis indicates distance away from the center of the circular TX. Red indicates high intensity and blue indicates low intensity. Rayleigh distance is at 14.58 mm.

case when depth is on the same order as or less than both the TX and RX diameters. Essentially, as the RX gets closer to the TX, less of the total beam power is able to escape around the sides of the RX.

Larger diameter RXs are able to capture more of the total beam power and thus typically generate more power as shown in Figure 4-7. Power scales proportionally to RX area for incoming plane waves because the intensity profile on the RX face is uniform. Power does not scale proportionally for realistic wave profiles, as shown in Figure 4-8, because they do not produce a uniform intensity on the RX face. Additionally, acoustic standing waves must be accounted for. To clarify, the intensity profile in Figure 4-8 represents the intensity transmitted into the medium by the TX when no obstruction, such as a RX, is present in the medium. If time were stopped and the RX placed in the medium in front of the TX, the RX would be subject to the intensity field as exactly shown in Figure 4-8. If time were then resumed, some of that energy would enter the RX and some of it would be reflected back towards the TX. The reflected energy would return to the TX and would again be partially reflected back toward the RX, and then again to the TX, then RX, etc. This back and forth reflection is what this paper refers to as standing waves or reflection activity. In other words, the standing wave contribution to voltage and power comprises all of the energy that constructively or destructively passes into the RX that is in addition to the intensity field shown in Figure 4-8. The standing wave contribution is closely approximated by the fluctuation value (i.e., AC or small signal discussed above) of the depth data and the intensity profile contribution is closely approximated by the mean value (i.e., DC or large signal discussed above) of the depth data.

The second design graph is the depth fluctuation design graph and is demonstrated in Figure 4-9, The depth fluctuation design graph gives the voltage and power fluctuation that the load experiences when the RX depth changes by as little as $\Delta z/2$ to $3\Delta z/4$ and represents the AC signal of the depth data. Once again, each line represents a RX diameter from 1 mm (dark blue) to 10 mm (red). An example of how to read this graph is as follows: at 15 mm depth, the value of the red line (10 mm RX diameter) in the depth fluctuation red line at 15 mm depth has a value of about 0.65 V_{RMS}. This means that the greatest voltage fluctuation that the load will see is 35% of 0.65 V_{RMS} or 0.2275 V_{RMS}. According to (4-1), the distance between fluctuation peaks is 0.8333 mm. This means the RX would have to voltage graph has a value of about 35%. In the depth magnitude voltage graph, the same move between 0.4167 mm to 0.625 mm ($\Delta z/2$ to $3\Delta z/4$) in the depth direction to experience

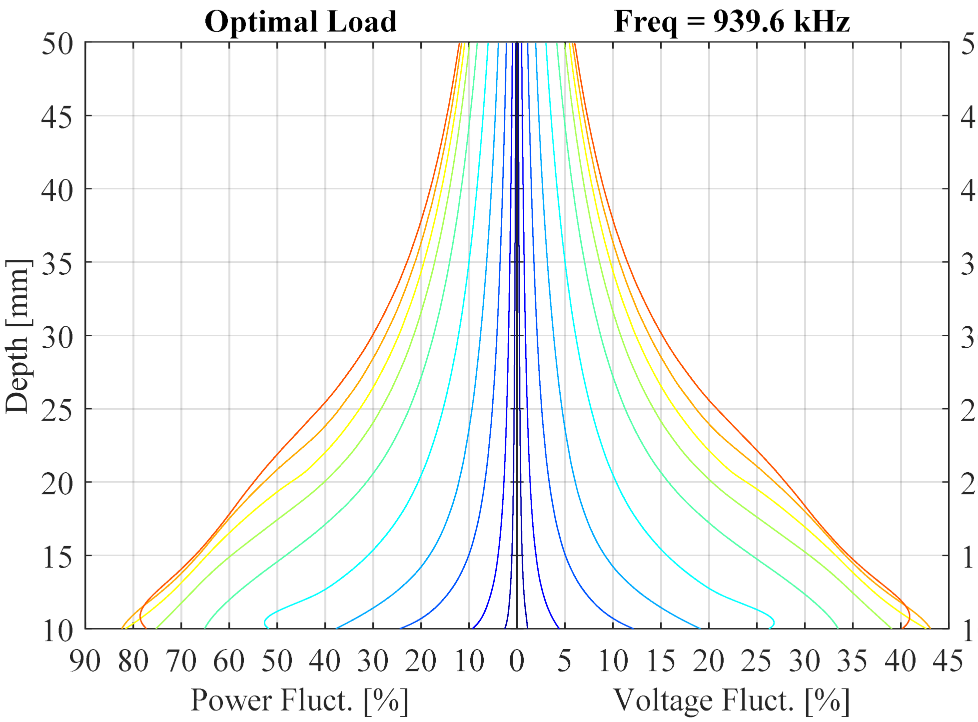

Figure 4-9. Depth fluctuation design graph. Voltage and power fluctuation percent as a function of depth for a TX and RX operating at 939.6 kHz and a fixed-average optimal load. Each line represents a RX diameter from 1 mm (dark blue) to 10 mm (red).

a 0.2275 V_{RMS} fluctuation. The data in Figure 4-9 show that the magnitude of voltage and power fluctuation significantly increases for shallower depths and larger RX diameters. This is due to increased reflection activity that is able to occur between the TX and RX when the transducers are relatively close together. Closeness in this case is defined as depth relative to the TX and RX diameter. For example, a 10-mm diameter TX and RX separated by a depth of 10 mm both appear to be one diameter away from each other. If the RX diameter were 5 mm, the RX would then appear to be two diameters away and thus apparently farther away than the 10-mm diameter RX. When considering this condition in terms of ray tracing, closer means that it is more difficult for pressure rays to stray. It should also be noted that if the RX were perfectly acoustically matched to the medium, no reflection activity would occur and thus voltage and power fluctuation would be zero.

4.6 Angle

The third parameter of interest is angle. As the angle between the TX and RX faces increases, three changes occur: 1) the reflection activity between the TX and RX decreases, 2) the effective reflection coefficient at the RX face increases, and 3) the pressure profile on the RX face changes. All of these changes contribute to a decrease in voltage and power. To visualize the combined effect of these changes, an angle profile is created by measuring load voltage and power as angle is varied for a fixed depth and zero offset. Figure 4-10 gives voltage and power angle profiles for depths between a valley (at 13.78 mm depth) and a peak (at 14.22 mm depth) for a 10-mm diameter TX and RX operating at 939.6 kHz. The graph shows that as angle increases, both voltage and power decrease. Change 1, a decrease in reflection activity, is easily noted by observing that the peak and valley lines

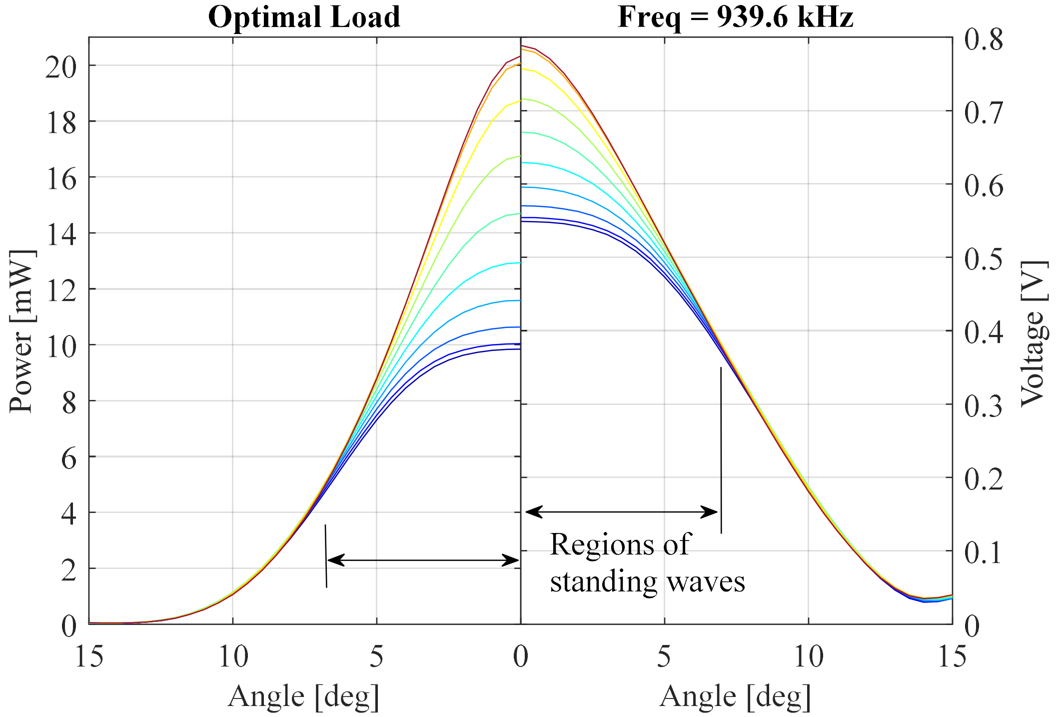

Figure 4-10. Voltage and power angle profile for a 10-mm diameter TX and RX operating at 939.6 kHz. Each line represents a fixed depth from 13.78 mm (dark blue) to 14.22 mm (red). The 13.78-mm line represents a valley and the 14.22-mm line represents a peak.

have very different values at 0°. Between 0° and 7°, acoustic standing waves form between the TX and RX to create the peaks and valleys discussed in the Depth section of this paper. At around 7°, acoustic standing waves are unable to form, so the peaks and valleys completely disappear. Change 2, a decrease in reflection coefficient, is described by considering the analytical relation given in (4-2) where R is the reflection coefficient, θ_i is the incident angle at which a pressure ray strikes the RX, θ_t is the transmitted angle of the pressure ray into the titanium matching layer, Z_{RX} is the acoustic impedance of the RX with attached load, and Z_m is the acoustic impedance of the medium which is the density times the speed of sound. Figure 4-11 illustrates the reflection coefficient and transmitted angle

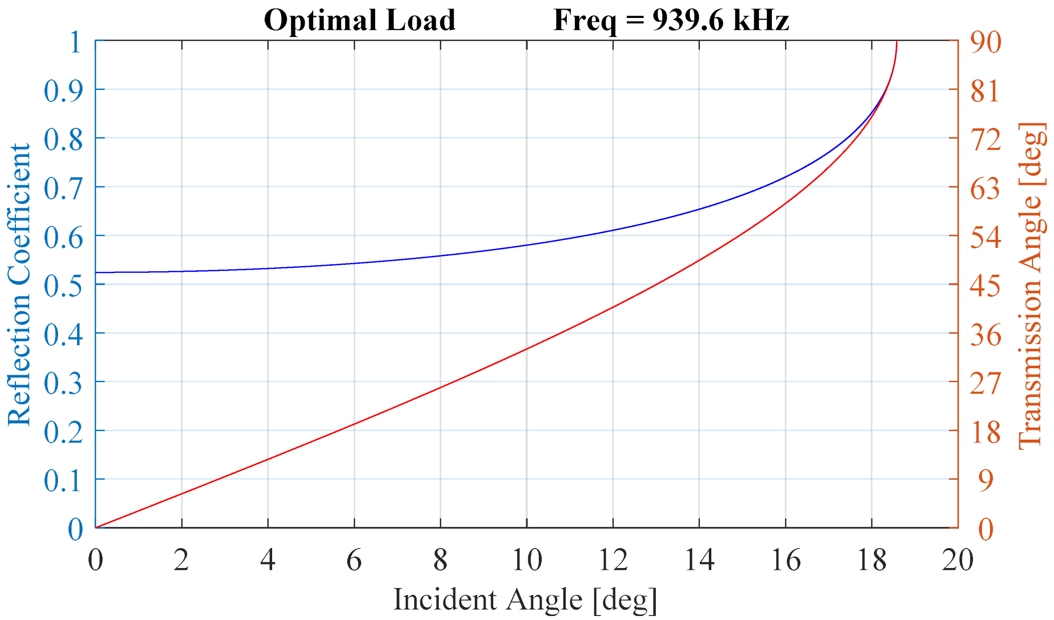

Figure 4-11. Reflection coefficient and transmission angle into the RX titanium matching layer of a single pressure ray as a function of incident angle for a 10-mm diameter RX operating at 939.6 kHz. Critical angle shown at 18.5°.

for a single pressure ray striking a 10-mm diameter RX at 939.6 kHz. The RX acoustic impedance is 5.367 MRayls in this case. It is observed that the reflection coefficient is about 0.52 for normal incidence and 1 at about 18.5° incident angle. It should be noted that not all of the pressures rays strike the RX at the same angle in realistic wave profiles as shown in Figure 4-12. This means that the reflection coefficient must be considered in the aggregate of pressure rays to determine its total effect on voltage and power. Change 3, a change in RX face pressure profile can be observed in Figure 4-13. As the RX is misoriented, vertical bands of high and low pressure appear on the RX face. The distance between these bands along the propagation axis is Δz, or half the wavelength in the medium. These bands appear in a similar fashion in the near-field and in the far-field. As the RX gets very close to the TX, the bands appear to be overlapped with a slight ripple

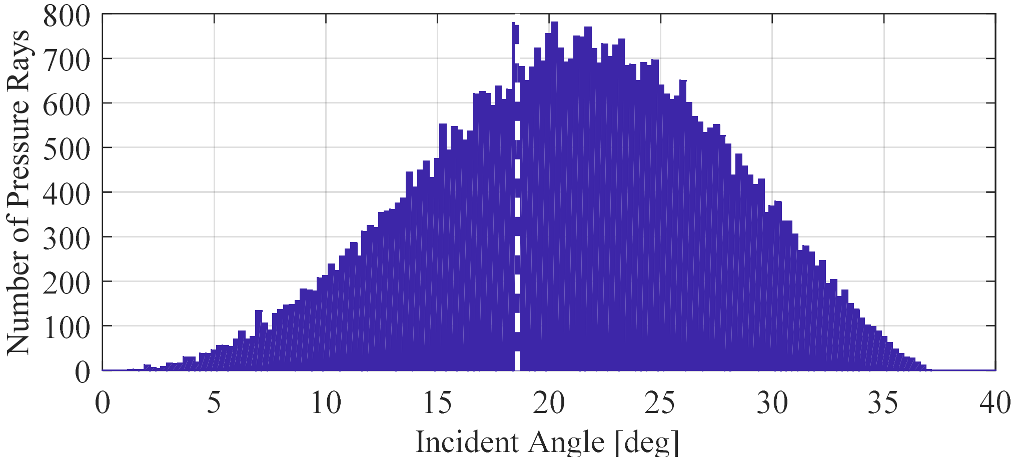

Figure 4-12. Histogram of pressure ray incident angles at the RX face for a 10-mm diameter TX and RX operating at 939.6 kHz and discretized with 226 elements each. The RX is positioned at 28.38 mm depth and oriented 20° relative to the TX. The critical angle of 18.5° is shown as the white dashed line.

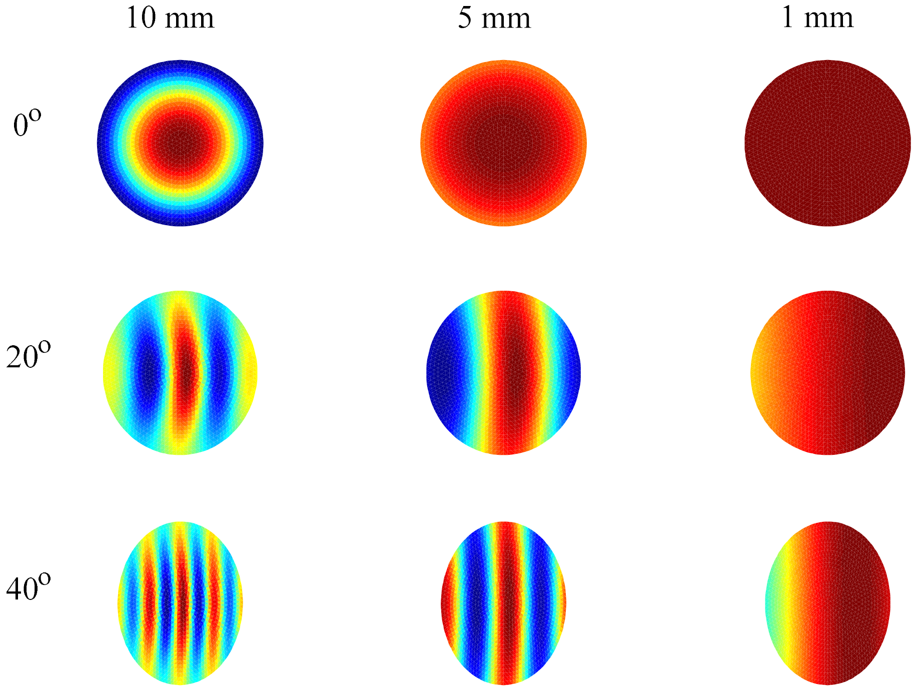

Figure 4-13. RX face pressure profiles for a 10-mm diameter TX operating at 939.6 kHz and a RX with 10, 5, and 1 mm diameter oriented at 0°, 20°, and 40°. The profiles are taken at 28.38 mm depth. Red represents high pressure and blue low pressure.

because of high reflection activity that is able to occur. As the RX gets very far away from the TX, the bands are more sharply defined because of the lack of reflection activity. At 1-mm RX diameter in the figure, the bands do not make a significant appearance on the RX face because the RX diameter is on the same order as the band spacing, $\Delta\mathbb{z}$.

$$R = \frac{\frac{Z_{RX}}{\cos(\theta_t)} - \frac{Z_m}{\cos(\theta_i)}}{\frac{Z_{RX}}{\cos(\theta_t)} + \frac{Z_m}{\cos(\theta_i)}} \tag{4-2}$$

To compile the angle profiles that occur along the depth range of interest (10 mm to 50 mm), like those in Figure 4-10, into a more broadly useful format: 1) Voltage and power angle profiles are generated for fixed depths. The depths of most interest are the peaks and valleys of the depth profile. The voltage and power angle profiles at peaks and valleys from a 10-mm diameter TX and RX operating at 939.6 kHz are given in Figure 4-14. These profiles are expressed as a percentage of the voltage and power at 0° angle, 0 mm offset, and the corresponding fixed depth. This means that at 0° angle, the voltage and power percentage is always 100%. In Figure 4-14, the dark blue line represents the angle profile at a peak or valley nearest to 10 mm depth and the dark red line represents the angle profile at a peak or valley nearest to 50 mm depth. It is notable that the acoustic standing waves change the shape of the peak and valley angle profiles. 2) The angle at which each voltage or power angle profile intersects the half voltage or power line (dashed black line in Figure 4-14) is measured and used to create the half angle design graph.

The third design graph is the half angle design graph demonstrated in Figure 4-15. This graph gives the angle at which the load voltage or power will be half of the load voltage or power seen at 0° angle. This angle is referred to as the half angle. In the figure, each line represents a RX diameter from 1 mm (dark blue) to 10 mm (red). An example of

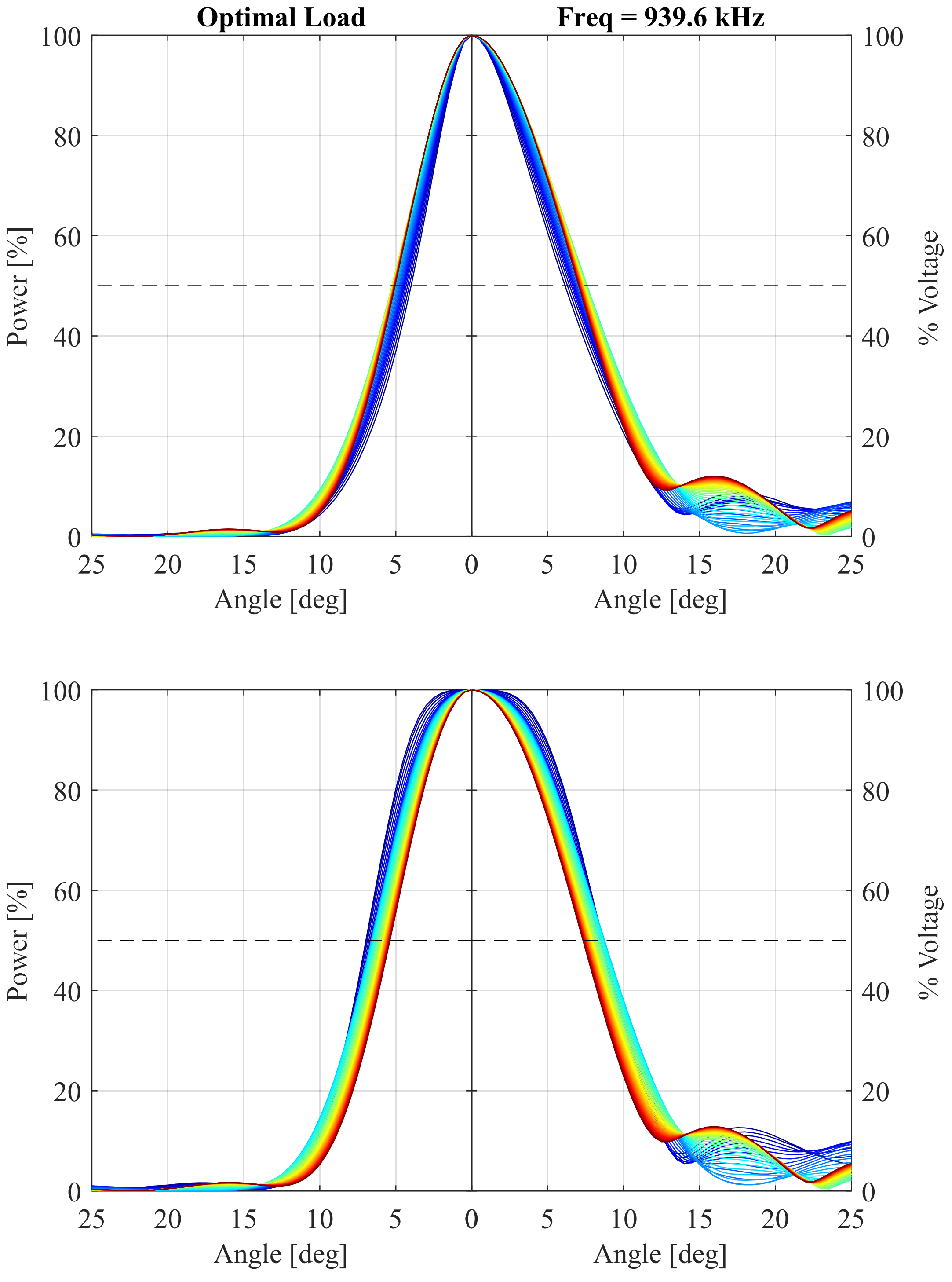

Figure 4-14. Angle profiles taken at peaks (top) and valleys (bottom) for a 10-mm diameter TX and RX operating at 939.6 kHz. Each line represents a fixed depth at a peak or valley from 10 mm (dark blue) to 50 mm (red). The angle at which each profile intersects the half voltage/power line is measured and used to create the half angle design graph.

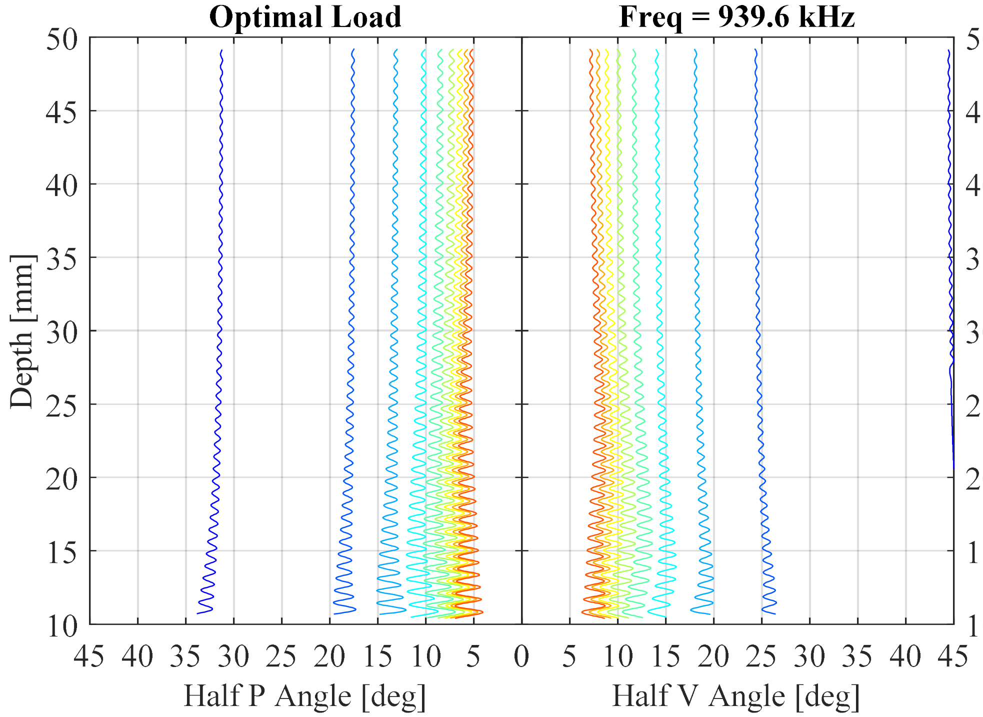

Figure 4-15. Half angle design graph for a 10-mm diameter TX operating at 939.6 kHz. Gives RX angle required to reduce the load voltage or power by half as a function of depth. Each line represents a RX diameter from 2 mm (dark blue) to 10 mm (red). far-field and partially into the near-field (Rayleigh distance is 14.58 mm in the figure).

how to the read this graph is as follows: at 45 mm depth, the half voltage angle of the red line (10 mm RX diameter) is about 7° and the half power angle is about 5°. This means that when the RX is at 45 mm depth, the load voltage will be reduced by half when the RX is misoriented by 7° and the power will be reduced by half when the RX is misoriented by 5°. The data in Figure 4-15 show that the half angle isn't a strong function of depth in the However, the half angle is a strong function of diameter. This is due to the band formation in the RX pressure profile as the RX is misoriented, as previously discussed. The oscillations in the half angle lines are due to acoustic standing waves and repeat at Δz intervals. These oscillations diminish as the RX gets farther away from the TX and as the acoustic impedance of the TX and RX approach the acoustic impedance of the medium.

4.7 Offset

The fourth parameter of interest is offset. Reflection activity is a function of the overlap and alignment of the TX and RX (i.e., offset at a fixed depth and 0° angle). Figure 4-16 is a depiction of TX and RX overlap as a function of offset. In the figure, the TX and RX are perfectly aligned when looking down the propagation axis at zero offset. When offset increases, as in the middle and right cases, the TX and RX become misaligned. The overlap of the TX and RX, depicted in green, represents the area in which high reflection activity occurs and in which acoustic standing waves form. Evidence of this is depicted in the offset profiles given in Figure 4-17. The figure gives voltage and power offset profiles for depths between a valley (at 13.78 mm depth) and a peak (at 14.22 mm depth) for a 10-mm diameter TX and RX operating at 939.6 kHz. In the figure, the peak (red) and valley (dark blue) lines converge to the same value (meaning no standing waves) as they approach 10 mm offset (offset at which there is no overlap between the TX and RX). To analyze the

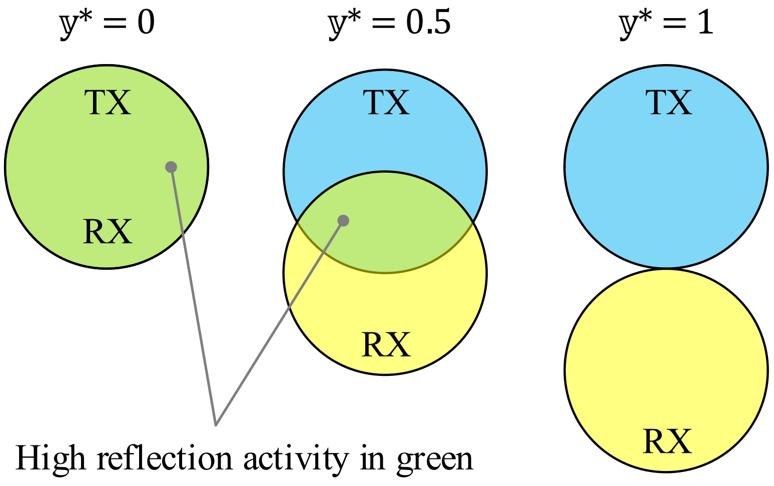

Figure 4-16. A depiction of reflection activity, shown in green, as a function of alignment (offset) between the TX and RX. The blue area represents the TX, the yellow area represents the RX, and the green area represents the overlap of TX and RX when looking down the propagation axis.

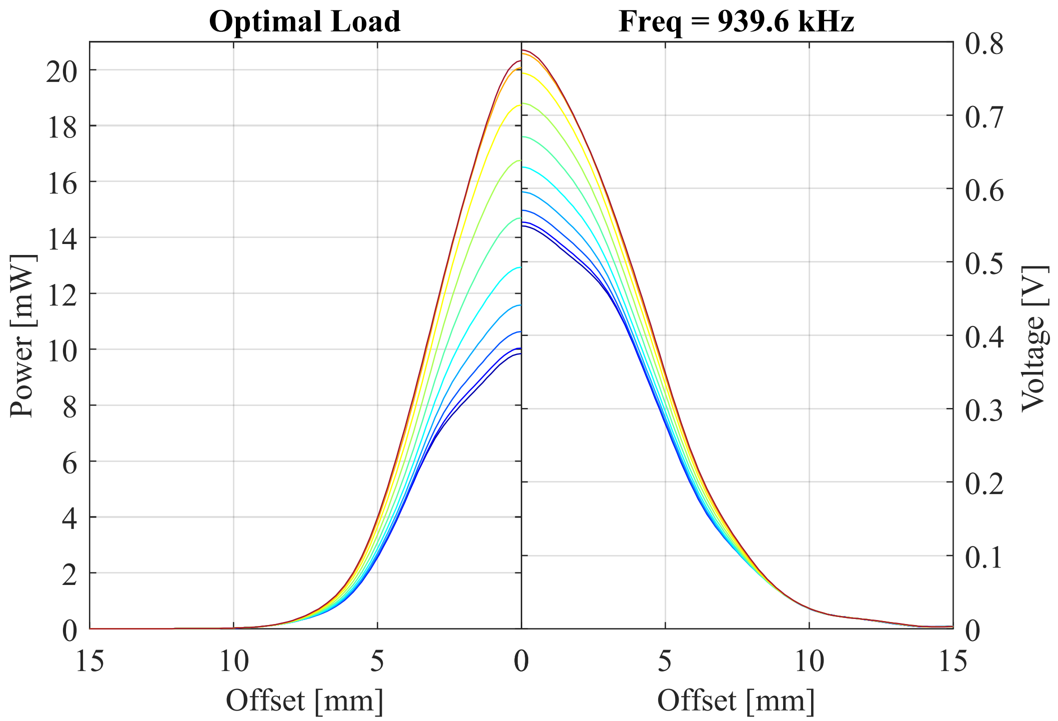

Figure 4-17. Voltage and power offset profile for a 10-mm diameter TX and RX operating at 939.6 kHz. Each line represents a fixed depth from 13.78 mm (dark blue) to 14.22 mm (red). The 13.78-mm line represents a valley and the 14.22-mm line represents a peak.

offset profiles from a broader point of view, normalized offset profiles are generated for each peak and valley between 10 mm and 50 mm depth in the same manner as described in the Angle section of this paper. A sample of these profiles for a 10-mm diameter TX and 3-mm diameter RX is given in Figure 4-18. This figure is provided to clarify that when the RX diameter is smaller than the TX diameter and the RX is in the near-field, the voltage and power at zero offset and angle is not always the maximum value of the profile. This is due to the interference pattern in the near field that can have low intensity magnitudes near to the propagation axis and high intensity magnitudes offset from the propagation axis as shown in Figure 4-8 at about 0.2 mm, 2.3 mm, and 7 mm depths. Nevertheless, the half voltage and power lines are still calculated as being half of the value at zero offset and zero

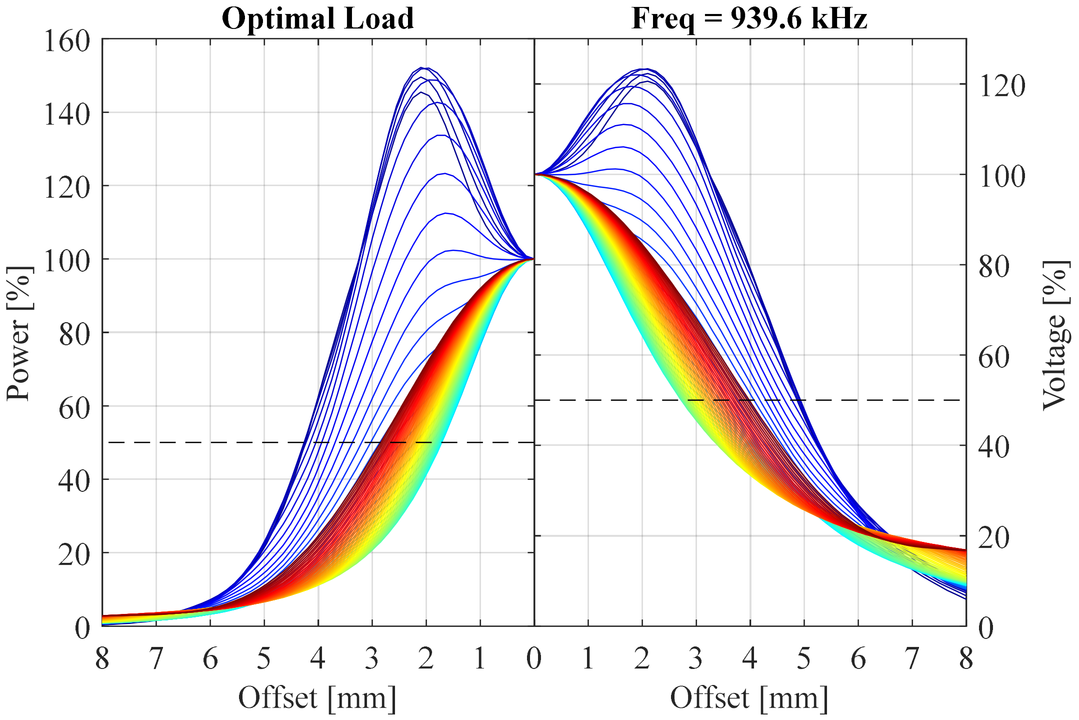

Figure 4-18. Offset profiles taken at peaks for a 10-mm diameter TX and 3-mm diameter RX operating at 939.6 kHz. Each line represents a fixed depth at a peak from 10 mm (dark blue) to 50 mm (red).

angle. The offset at the intersection of these lines and the offset profile is measured and compiled into the half offset design graph.

The fourth design graph is the half offset design graph demonstrated in Figure 4-19. The half offset design graph gives the offset at which the load voltage or power will be reduced to half of the load voltage or power seen at zero offset. This offset is referred to as the half offset. In the figure, each line represents a RX diameter from 1 mm (dark blue) to 10 mm (red). An example of how to the read this graph is as follows: at 20 mm depth, the half voltage offset of the green line (6 mm RX diameter) is about 4 mm and the half power offset is about 2.7 mm. This means that when the RX is at 20 mm depth, the load voltage will be reduced by half when the RX is misaligned by 4 mm and the load power will be

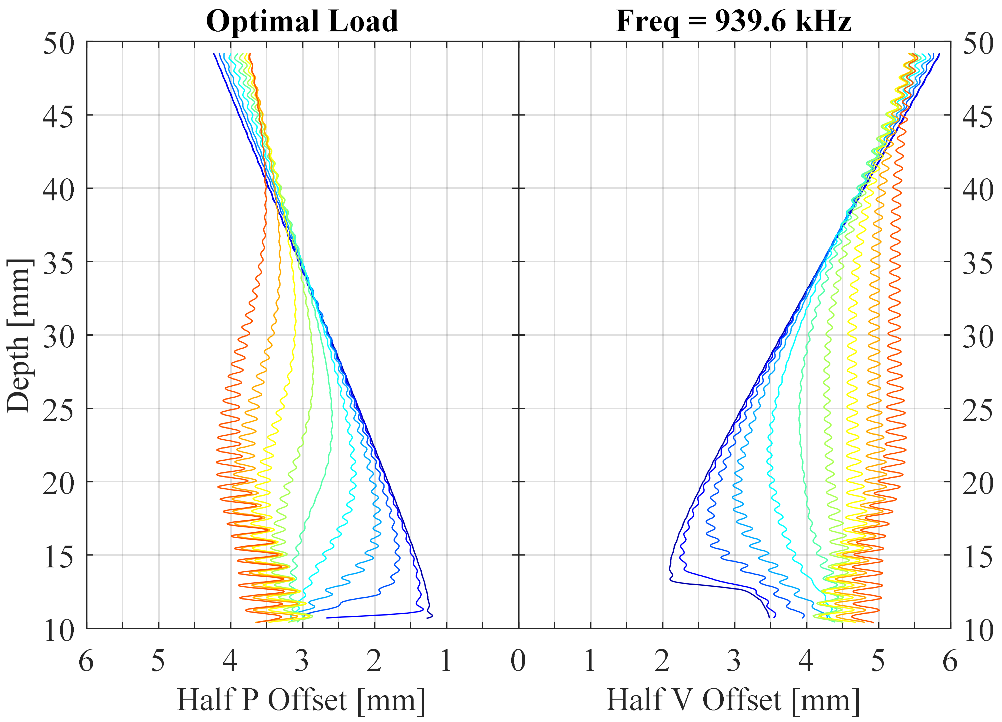

Figure 4-19. Half offset design graph for a 10-mm diameter TX operating at 939.6 kHz. Gives RX offset required to reduce the load voltage or power by half as a function of depth. Each line represents a RX diameter from 1 mm (dark blue) to 10 mm (red).

reduced by half when the RX is misaligned by 2.7 mm. The half offset dark blue line, in Figure 4-19, appears to be diverging from the propagation axis at a nearly constant angle. This divergence angle can be approximated in the far-field for RX diameters that are small relative to the TX diameter by calculating the directivity of the acoustic beam as given in (4-3) [28], where H is the directivity of the acoustic beam emitted from the TX, k is the wave number, a is the radius of the TX and ϕ is the angle relative to the propagation axis. In the half voltage offset graph, the divergence angle is calculated by setting H equal to 0.5 and solving for ϕ. In the half power offset graph, the divergence angle is calculated by setting H^2 equal to 0.5 and solving for ϕ. A comparison of calculated divergence angles and measured divergence angles from 6 sets of half voltage and power offset graphs yielded a mean 4.2% error with 1.32% standard deviation. The measurements from simulation data were taken using a 1-mm diameter RX, 10-mm diameter TX, and frequencies from 600 kHz to 1350 kHz in increments of 150 kHz. All of the measured angles were smaller than the calculated divergence angles. When approximating or measuring the divergence angle, it should be noted that the line of the divergence angle does not pass through the center of the TX face. For RX diameters that are of similar size to the TX, a divergence angle does occur but takes longer to form and is smaller than the calculated divergence angle as shown in the extended half offset design graph in Figure 4-20. In the figure, it is notable that the data trends appear slightly different than in Figure 4-19. This is due to differences in the Rayleigh distance. In Figure 4-19 the Rayleigh distance is 14.58 mm while it is 6.67 mm in Figure 4-20. The data trends in Figure 4-19 are similar to the data trends to Figure 4-20 but are effectively stretched by a factor 14.58/6.67 = 2.19 in the depth direction.

$$\mathrm{H} = \frac{2J_1(ka\sin(\phi))}{ka\sin(\phi)} \tag{4-3}$$

It is important to note that the effects of angle misorientation and offset misalignment do not linearly superimpose. When the RX is offset from the propagation axis, the intensity seen on the RX face is no longer axially symmetric. For example, the power delivered to the load for a 10-mm TX and RX operating at 469.8 kHz and 20 mm depth experiences a 40.7% reduction for a 3-mm offset and a 16.6% reduction for a 5° angle separately. At a combined 3-mm offset and +5° angle, the power is reduced by 32.5%. At a combined 3-mm offset and -5° angle, the power is reduced by 63.5%. Neither of these percentages correspond to the superposition combined reduction of 49.5%.

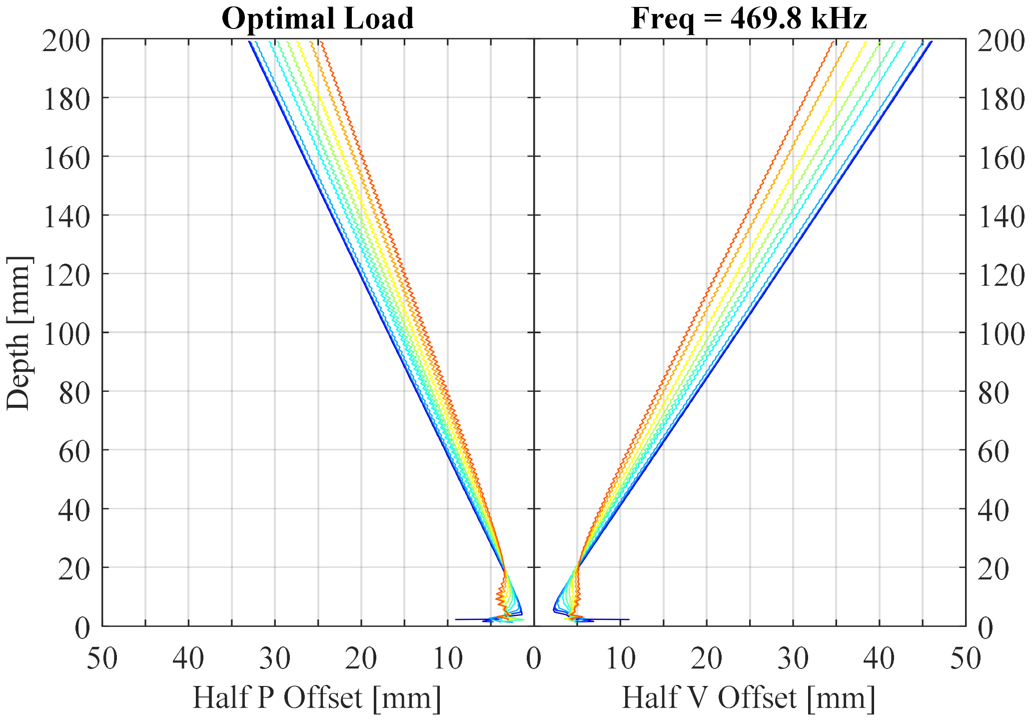

Figure 4-20. Extended half offset design graph at 469.8 kHz. Each line represents a RX diameter from 1 mm (dark blue) to 10 mm (red).

4.8 Nondimensional Analysis

To apply the four design graphs developed in this paper to a wider range of dimensional system parameters, nondimensional parameters and design graphs are presented in this section. Table 4-3 provides a reference of nondimensional expressions for system parameters. The variables used are consistent with the variables in Chapter 3 and are summarized as follows: $\mathbb{z}$ is the depth or axial separation distance between the TX and RX, θ_X is the angle between the TX and RX faces, $\mathbb{y}$ is the offset or lateral offset distance between the TX and RX, D_{TX} is the diameter of the TX, D_{RX} is the diameter of the RX, f is the operating frequency of the TX, c is the speed of sound in the medium, λ is the acoustic wavelength in the medium, R_L is the impedance of the load, $R_{L,opt,avg}$ is the fixed-average

Table 4-3. Assignment of variables to system parameters with accompanying nondimensional expressions.

Parameter	Variable	Nondimensional Expression
TX Diameter	D_{TX}	$D_{TX}^* = D_{TX}/D_{TX} = 1$
RX Diameter	D_{RX}	$D_{RX}^* = D_{RX}/D_{TX}$
Depth	$\mathbb{z}$	$\mathbb{z}^* = \mathbb{z}/D_{TX}$
Angle	θ_X	θ_X
Offset	$\mathbb{y}$	$\mathbb{y}^* = \mathbb{y}/D_{TX}$
Frequency	f	$f^* = D_{TX}/\lambda = fD_{TX}/c$
Load Impedance	R_L	$R_L^* = R_L/R_{L,opt,avg}$
RMS Voltage	V	$V^* = V/D_{TX}$
Avg. Power	P	$P^* = P/D_{TX}^2$

optimal load resistance, V is the RMS voltage measured across the RX load, and P is the average power delivered to the RX load. The nondimensional expressions given in Table 4-3 are defined as follows: all length dimensions in the system are nondimensionalized with respect to the TX diameter and the RX load is nondimensionalized with respect to the fixed-average optimal load impedance. The TX diameter is chosen as the nondimensional length parameter because its value, along with wavelength, determine the emitted acoustic beam pattern. The beam pattern, in turn, determines the sensitivity of voltage and power to depth, angle, and offset.

The four types of design graphs previously explained are generated using the sweep range of nondimensional parameters given in Table 4-4. The table additionally provides the dimensional parameters used to create the nondimensional graphs. Even though dimensional parameters are used to create the design graphs, the data hold for any actual dimensions. The nondimensional set of design graphs can be converted to dimensional units by using the relationships found in Table 4-3. The design graphs should be

Table 4-4. Parameter sweep values considered in this paper given in nondimensional parameters (top half). Actual dimensional values used to generate design graphs (bottom half).

Parameter	Var	Units	Min	Incr	Max
Depth*	$\mathbb{z}^*$	–	1	$1/30f^*$	5
Offset*	$\mathbb{y}^*$	–	0	0.015	1.5
RX Diameter*	D_{RX}^*	–	0.1	0.1	1
Frequency*	f^*	–	3	3	9
Load*	R_L^*	–	1	1	1
Depth	$\mathbb{z}$	mm	10	$c/(30f)$	50
Angle	θ_X	deg	0	0.5	45
Offset	$\mathbb{y}$	mm	0	0.15	15
TX Diameter	D_{TX}	mm	10	–	10
RX Diameter	D_{RX}	mm	1	1	10
Frequency	f	kHz	469.8	469.8	1409.4

regenerated if assuming different piezoelectric properties, transducer layers, layer thickness ratios, or medium properties than assumed in this paper. The thickness ratio of the transducers assumed in this paper are 0.45. This means that the piezo layer is 45% of the total transducer thickness (piezo layer plus titanium layer). The nondimensional design graphs that follow provide additional insights about the effect that frequency plays in voltage and power.

The nondimensional depth magnitude design graphs are given in Figure 4-21. Each of the figures represents a different frequency (a higher value of f^* means a higher frequency) and all figures assume optimal load. The lines in each of the graphs correspond to a nondimensional RX diameter, D_{RX}^*, from 0.1 (dark blue) to 1 (red). A nondimensional RX diameter of 0.1 means that the dimensional RX diameter is 10% of the TX diameter. In the figures, it is observed that an increase in frequency has the general effect of

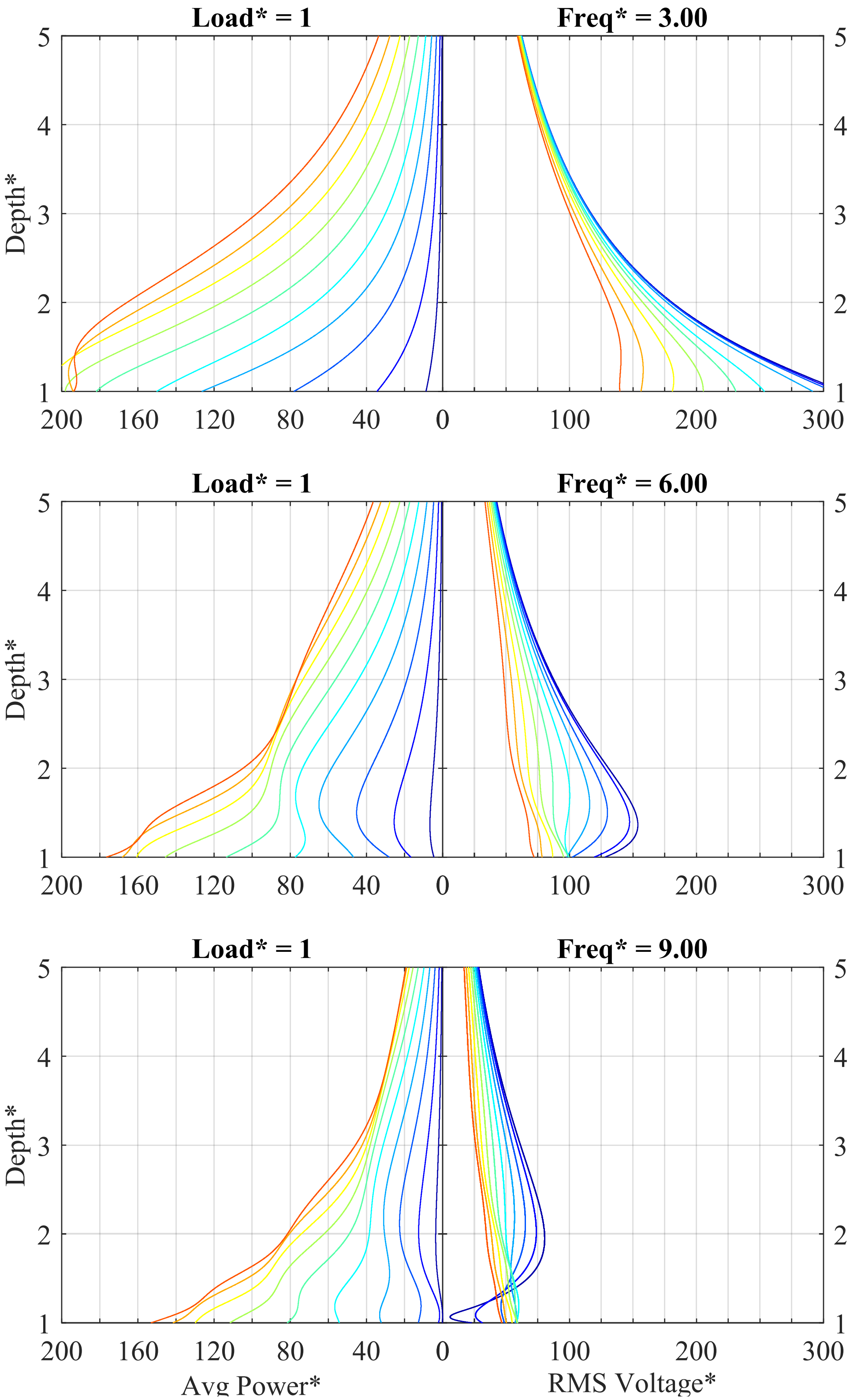

Figure 4-21. Nondimensional depth magnitude design graphs. Each line represents D_{RX}^* from 0.1 (dark blue) to 1 (red).

decreasing both power and voltage. This is due to the high absorption coefficient of the assumed medium properties. A general effect of increased frequency in the design graphs is the increase in the Rayleigh distance. As previously discussed, a change in Rayleigh distance has the effect of stretching the data trends in the depth direction as frequency is increased. Before extracting data from the depth magnitude design graph, it is important to note that the final average power dimensional value must be multiplied by a scaling correction factor as given in Figure 4-22. The correction factor is numerically generated by compiling data from multiple scaled design graphs into a correction band that is valid for all values in the depth magnitude design graphs. The correction factor does not need to be applied to the final dimensional RMS voltage because its correction factor is approximately one for all TX diameters. An example of how to extract dimensional values from the

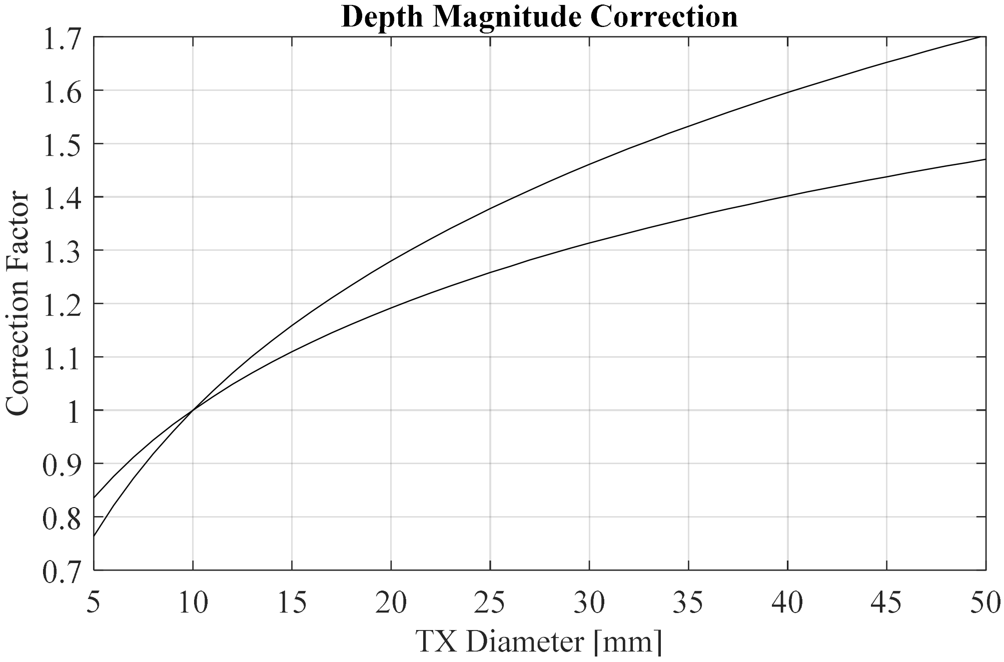

Figure 4-22. Correction factor for nondimensional depth magnitude design graph. The two lines represent the upper and lower limits of correction certainty.

nondimensional depth magnitude design graphs is as follows: a 12.7-mm diameter TX and 6.35-mm diameter RX operating at 1110 kHz are placed 20 mm apart. RX Diameter* (D_{RX}^{*}) is calculated as 12.7/6.35 = 0.5 which corresponds to the cyan lines. Frequency* (f^{*}) is calculated as 1110000*0.0127/1566 =9.00 which corresponds to the bottom graph. Depth* ($\mathbb{z}^{*}$) is calculated as 20/12.7 = 1.57. The correction factor from Figure 4-22 for a 12.7-mm diameter TX is found to be about 1.07. The depth magnitude design graph in Figure 4-21 (bottom graph, cyan line) gives about 54 for RMS Voltage* (V^{*}) and about 46 for Avg. Power* (P^{*}). In dimensional form, this gives the mean magnitude as 54*0.0127 = 0.686 V_{RMS} and 46*0.0127^2*1.07 = 0.00794 W = 7.94 mW for 7200 W/m^2 intensity emitted from the TX face. To put this in terms of efficiency, 7200*π*0.0127^2/4 = 91.2 mW is emitted into the medium by the TX which means that the system efficiency is 7.86/91.2 = 8.7%.

The nondimensional depth fluctuation design graphs are given in Figure 4-23. Upon close inspection, these graphs are also subject to Rayleigh distance stretching and medium absorption. When converting depth fluctuation design graph data to dimensional units, a correction factor is first obtained from Figure 4-24 based on the TX diameter. From the figure, the correction factor for a 12.7-mm diameter RX is found to be about 0.9. Unlike the depth magnitude correction factor, the depth fluctuation correction factor must be applied to voltage and power fluctuation dimensional values. Continuing the example from the previous paragraph, the bottom graph and cyan lines are consulted. The corresponding voltage fluctuation is about 21% and the power fluctuation is about 42%. As an intermediate step, the half wavelength in the medium ($\Delta\mathbb{z}$) is calculated as $1566/1110000/2 = 0.705\ \mathrm{mm}$. Converting to dimensional form, the RX experiences a

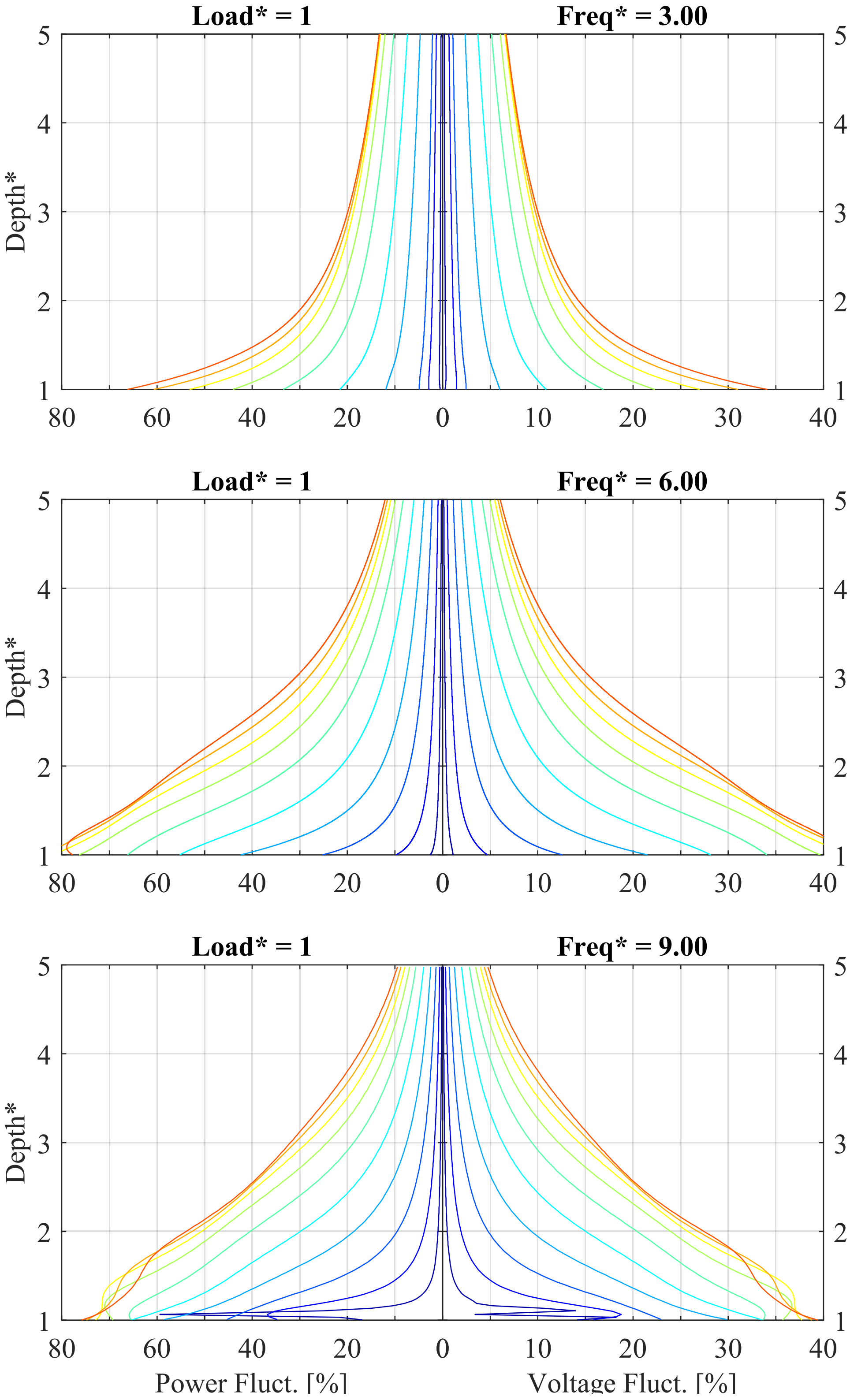

Figure 4-23. Nondimensional depth fluctuation design graphs. Each line represents D_{RX}^{*} from 0.1 (dark blue) to 1 (red).

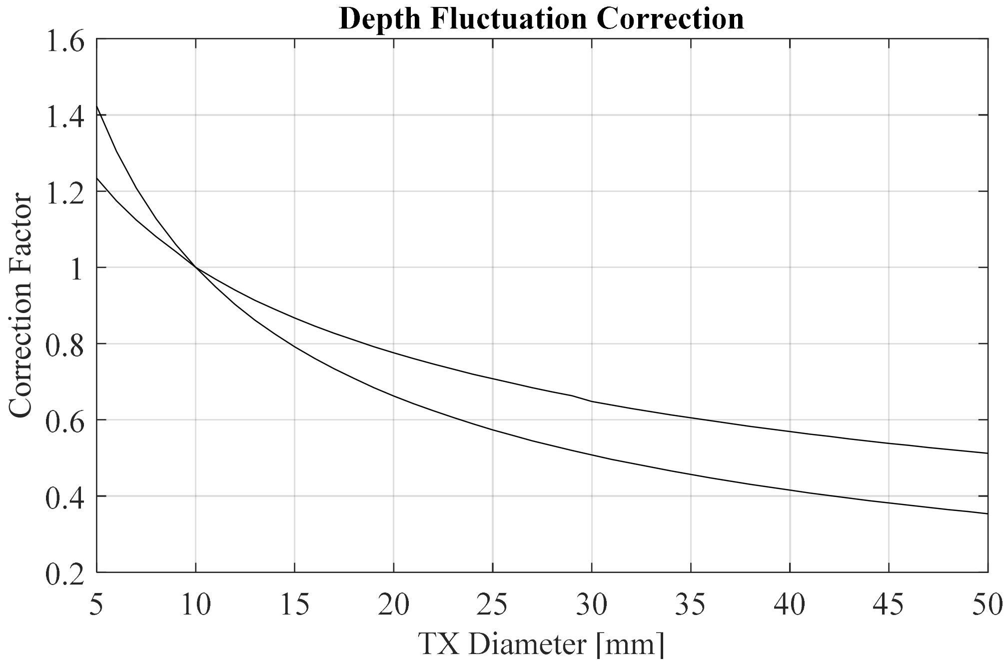

Figure 4-24. Correction factor for nondimensional depth fluctuation design graph. The two lines represent the upper and lower limits of correction certainty.

maximum voltage fluctuation of 0.21*0.686*0.9 = 0.13 V_{RMS} and a power fluctuation of 0.42*7.86*0.9 = 2.97 mW when its position is disturbed in the depth direction by as little as 0.705/2 = 0.353 mm to 3*0.705/4 = 0.529 mm.

The nondimensional half angle design graphs are given in Figure 4-25. The half angle is observed to be a strong function of frequency. As discussed in the Angle section of this paper and illustrated in Figure 4-13, pressure bands form on the RX face as angle increases. The spacing of the bands is $\Delta \mathbb{z}$ in the depth direction, which is a function of frequency. As frequency increases, the bands appear at smaller RX angles, thus increasing the sensitivity of voltage and power to disturbances in RX angle. It should be noted that unlike the depth magnitude and depth fluctuation design graphs, the half angle design graph does not require a correction factor. However, the amplitude of the oscillations in the half angle lines increases/decreases with an increase/decrease in voltage and power fluctuation

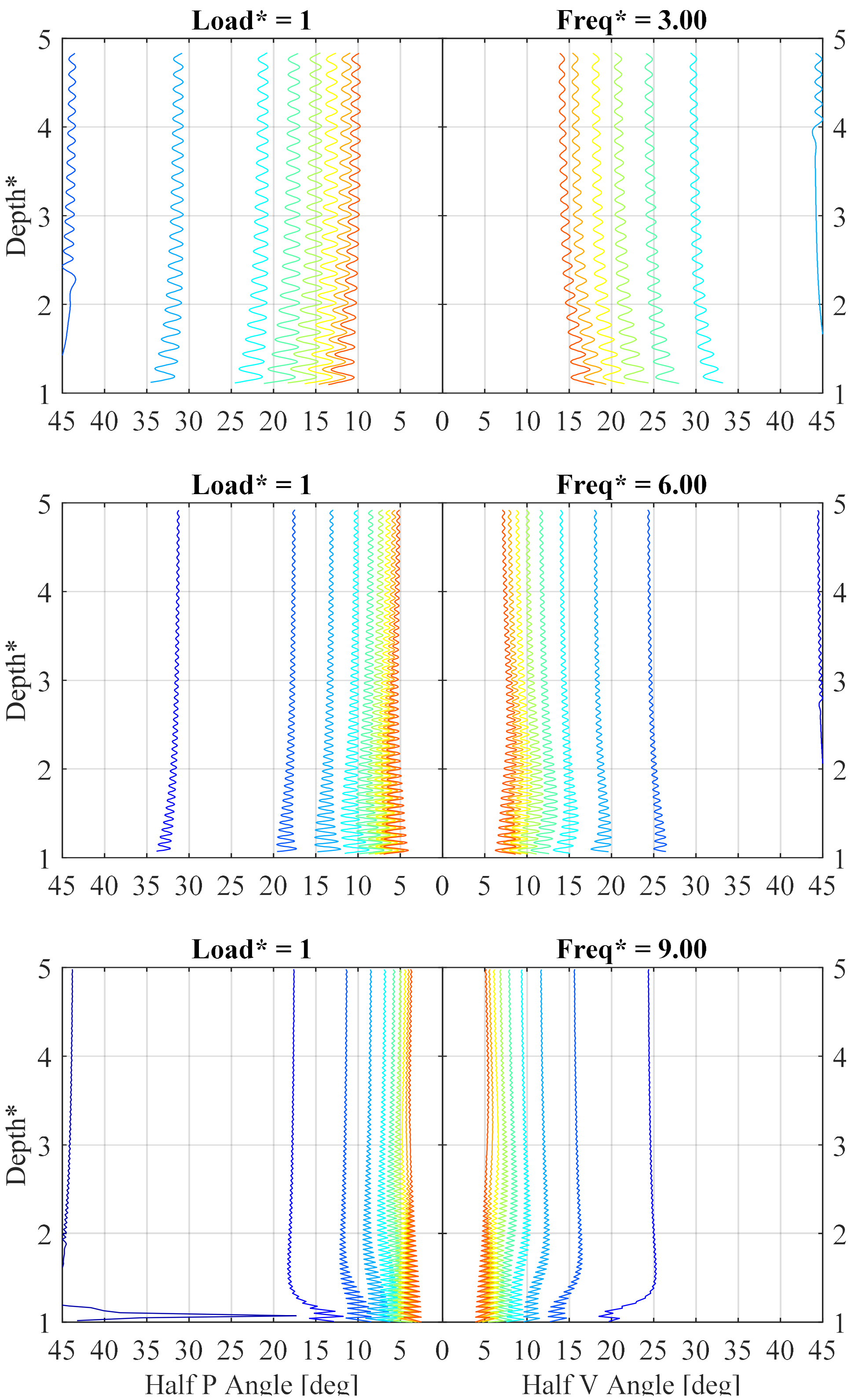

Figure 4-25. Nondimensional half angle design graphs. Each line represents D_{RX}^{*} from 0.1 (dark blue) to 1 (red).

percent. Continuing the example from the previous paragraphs, the bottom graph and cyan lines are consulted. The corresponding half voltage angle is about 8.9° and the half power angle is about 6.3°. This means that the load voltage is reduced to 0.686/2 = 0.343 V_{RMS} at an 8.9° disturbance in RX orientation, and the power is reduced to 7.86/2 = 3.93 mW at a 6.3° disturbance.

The nondimensional half offset design graphs are given in Figure 4-26. The half offset is a strong function of frequency. Higher frequencies result in a narrower beam, which decreases the divergence angle of the half offset lines as discussed in the Offset section of this paper. This means that voltage and power are more sensitive to disturbances in angle at higher frequencies. Another way of considering this effect is to observe that higher frequencies increase the Rayleigh distance, which effectively stretches the half offset line trends in the depth direction. The half offset design graphs, like the half angle design graphs, do not require a correction factor and the amplitude of the half offset line oscillations increases with an increase in voltage and power fluctuation. Continuing the example from the previous paragraphs, the bottom graph and cyan lines are once again consulted. The corresponding half voltage offset is about 0.43 and the half power offset is about 0.315. This means that the load voltage is reduced to 0.686/2 = 0.343 V_{RMS} at a 0.43*12.7 = 5.46 mm disturbance in RX alignment, and the power is reduced to 7.86/2 = 3.93 mW at a 0.315*12.7 = 4 mm disturbance.

4.9 Conclusion

This paper provided an analysis of load voltage and power magnitude and sensitivity to disturbances in RX depth, orientation, and alignment. The dependence of

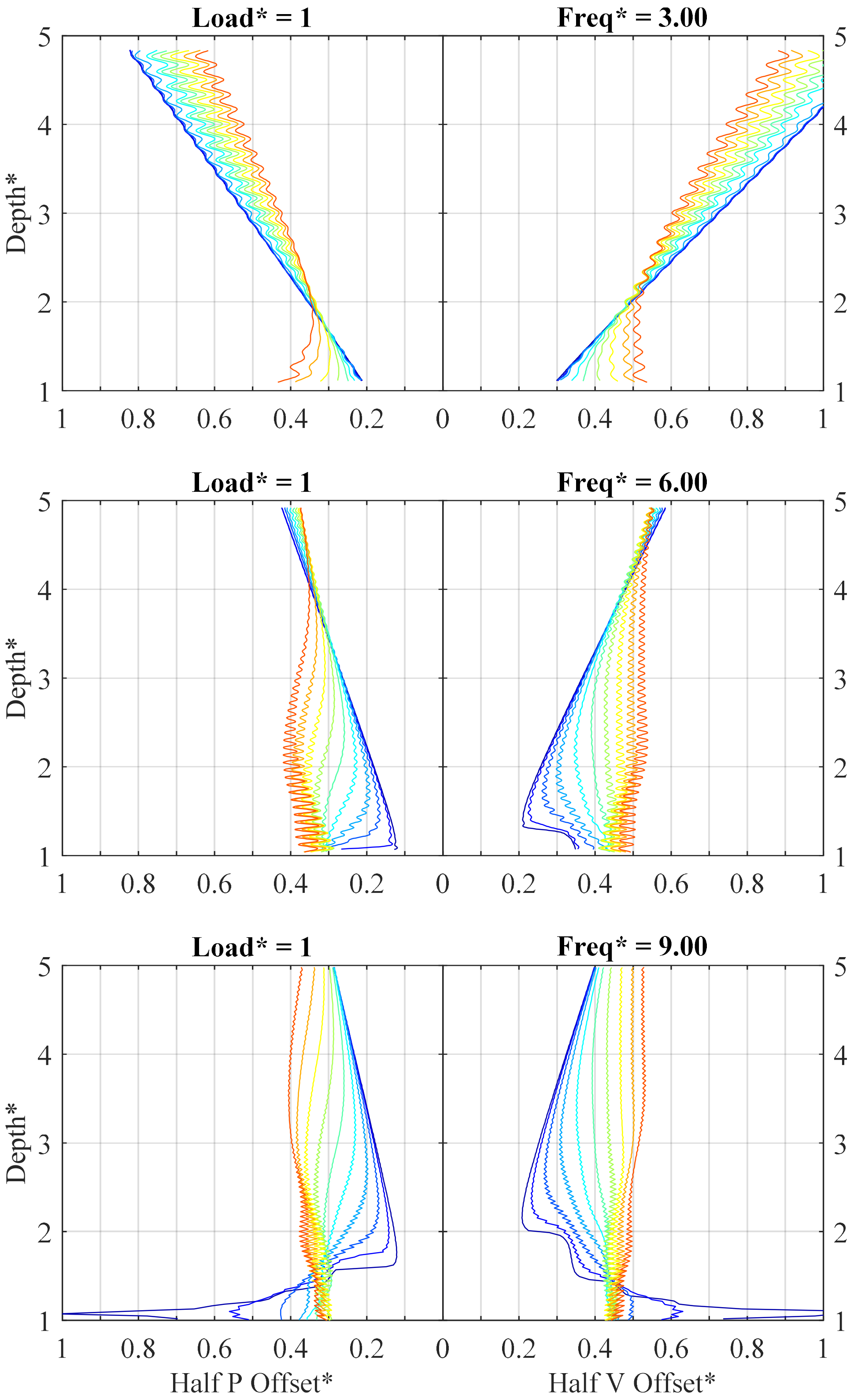

Figure 4-26. Nondimensional half offset design graphs. Each line represents D_{RX}^{*} from 0.1 (dark blue) to 1 (red).

voltage and power on load, diameter, and operating frequency was also explored. Four types of design graphs were developed: depth magnitude, depth fluctuation, half angle, and half offset. The depth magnitude design graph provides details about the mean voltage and power as a function of depth. The depth fluctuation design graph provides the maximum change in voltage and power the load will experience for a depth disturbance of at least $\Delta\mathbb{z}/2$ to $3\Delta\mathbb{z}/2$. The half angle and offset graphs provide the angle and offset at which the voltage and power will be reduced to half of its zero-angle-zero-offset value. Nondimensional analysis and graphs were then provided to extend applicability to a wider range of scenarios. Correction factors were introduced to allow proper scaling of the nondimensional depth magnitude and fluctuation graphs.

4.10 Funding

The authors gratefully acknowledge funding from the National Science Foundation under grant number ECCS-1408265.

4.11 References

[1] H. Basaeri, D. B. Christensen, and S. Roundy, “A review of acoustic power transfer for bio-medical implants,” *Smart Mater. Struct.*, vol. 25, no. 12, pp. 1–23, 2016.

[2] H. Kawanabe, T. Katane, H. Saotome, O. Saito, and K. Kobayashi, “Power and information transmission to implanted medical device using ultrasonic,” *Jpn. J. Appl. Phys.*, vol. 40, no. 5, pp. 3865–3866, 2001.

[3] S.-N. Suzuki, S. Kimura, T. Katane, H. Saotome, O. Saito, and K. Kobayashi, “Power and interactive information transmission to implanted medical device using ultrasonic,” *Japanese J. Appl. Physics, Part 1 Regul. Pap. Short Notes Rev. Pap.*, vol. 41, no. 5 B, pp. 3600–3603, 2002.

[4] S. Arra, J. Leskinen, J. Heikkilä, and J. Vanhala, “Ultrasonic power and data link for wireless implantable applications,” in *International Symposium on Wireless*

Pervasive Computing, 2007, pp. 567–571.

[5] S. Ozeri and D. Shmilovitz, "Ultrasonic transcutaneous energy transfer for powering implanted devices.," *Ultrasonics*, vol. 50, no. 6, pp. 556–66, May 2010.

[6] A. Denisov and E. Yeatman, "Ultrasonic vs. inductive power delivery for miniature biomedical implants," in *Body Sensor Networks BSN 2010 International Conference on*, 2010, no. June, pp. 84–89.

[7] Y. Shigeta, Y. Hori, K. Fujimori, K. Tsuruta, and S. Nogi, "Development of highly efficient transducer for wireless power transmission system by ultrasonic," in *2011 IEEE MTT-S International Microwave Workshop Series on Innovative Wireless Power Transmission: Technologies, Systems, and Applications*, 2011, pp. 171–174.

[8] S. Ozeri, B. Spivak, and D. Shmilovitz, "Non-invasive sensing of the electrical energy harvested by medical implants powered by an ultrasonic transcutaneous energy transfer link," *IEEE Int. Symp. Ind. Electron.*, pp. 1153–1157, 2012.

[9] A. Sanni, A. Vilches, and C. Toumazou, "Inductive and ultrasonic multi-tier interface for low-power, deeply implantable medical devices.," *IEEE Trans. Biomed. Circuits Syst.*, vol. 6, no. 4, pp. 297–308, Aug. 2012.

[10] Y. Hori, K. Fujimori, K. Tsuruta, and S. Nogi, "Design and development of highly efficient transducer for ultrasonic wireless power transmission system," *IEEJ Trans. Electron. Inf. Syst.*, vol. 132, no. 3, pp. 337–343, 2012.

[11] S. Q. Lee, W. Youm, and G. Hwang, "Biocompatible wireless power transferring based on ultrasonic resonance devices," *Proc. Meet. Acoust.*, vol. 19, pp. 1–9, 2013.

[12] C. Mo, S. Hudson, and L. J. Radziemski, "Effect of misalignment between ultrasound piezoelectric transducers on transcutaneous energy transfer," vol. 8688, no. 509, p. 868814, 2013.

[13] D. Seo, J. M. Carmena, J. M. Rabaey, E. Alon, and M. M. Maharbiz, "Neural dust: an ultrasonic, low power solution for chronic brain-machine interfaces," no. April, 2013.

[14] S. Shahab and a Erturk, "Contactless ultrasonic energy transfer for wireless systems: acoustic-piezoelectric structure interaction modeling and performance enhancement," *Smart Mater. Struct.*, vol. 23, no. 12, p. 125032, 2014.

[15] Q. He, J. Liu, B. Yang, X. Wang, X. Chen, and C. Yang, "MEMS-based ultrasonic transducer as the receiver for wireless power supply of the implantable microdevices," *Sensors Actuators, A Phys.*, vol. 219, pp. 65–72, 2014.

[16] S. Q. Lee, W. Youm, G. Hwang, K. S. Moon, and Y. Ozturk, "Resonant ultrasonic wireless power transmission for bio-implants," vol. 9057, p. 90570J, 2014.

[17] S. Ozeri and D. Shmilovitz, “Simultaneous backward data transmission and power harvesting in an ultrasonic transcutaneous energy transfer link employing acoustically dependent electric impedance modulation,” *Ultrasonics*, vol. 54, no. 7, pp. 1929–1937, 2014.

[18] T. C. Chou, R. Subramanian, J. Park, and P. P. Mercier, “A miniaturized ultrasonic power delivery system,” *IEEE 2014 Biomed. Circuits Syst. Conf. BioCAS 2014 - Proc.*, pp. 440–443, 2014.

[19] H. Vihvelin, J. Leadbetter, M. Bance, J. A. Brown, and R. B. A. Adamson, “Compensating for tissue changes in an ultrasonic power link for implanted medical devices,” *IEEE Trans. Biomed. Circuits Syst.*, no. April, 2015.

[20] D. B. Christensen and S. Roundy, “Ultrasonically powered piezoelectric generators for bio-implantable sensors: Plate versus diaphragm,” *J. Intell. Mater. Syst. Struct.*, pp. 1–14, 2015.

[21] S. H. Song, A. Kim, and B. Ziaie, “Omni-directional ultrasonic powering for mm-scale implantable biomedical devices,” *Biomed. Eng. IEEE Trans.*, vol. 62, no. 11, pp. 1–14, 2015.

[22] J. Zhou, A. Kim, and B. Ziaie, “An ultrasonically controlled power management system for implantable biomedical devices,” *Biomed. Circuits Syst. …*, pp. 1–4, 2015.

[23] B. Fang, T. Feng, M. Zhang, and S. Chakrabartty, “Feasibility of B-mode diagnostic ultrasonic energy transfer and telemetry to a cm2 sized deep-tissue implant,” *Proc. - IEEE Int. Symp. Circuits Syst.*, vol. 2015–July, pp. 782–785, 2015.

[24] J. Charthad, M. J. Weber, T. C. Chang, and A. Arbabian, “A mm-sized implantable medical device (IMD) with ultrasonic power transfer and a hybrid bi-directional data link,” *IEEE J. Solid-State Circuits*, vol. 50, no. 8, pp. 1741–1753, 2015.

[25] L. Radziemski and I. R. S. Makin, “In vivo demonstration of ultrasound power delivery to charge implanted medical devices via acute and survival porcine studies,” *Ultrasonics*, vol. 64, pp. 1–9, 2016.

[26] D. Shmilovitz, S. Ozeri, C. C. Wang, and B. Spivak, “Noninvasive control of the power transferred to an implanted device by an ultrasonic transcutaneous energy transfer link.,” *IEEE Trans. Biomed. Eng.*, vol. 61, no. 4, pp. 995–1004, 2014.

[27] *Guidance for Industry and FDA Staff Information for Manufacturers Seeking Marketing Clearance of Diagnostic Ultrasound Systems and Transducers*. U.S. Department of Health and Human Services, Food and Drug Administration, Center for Devices and Radiological Health, 2008.

[28] D. A. Christensen, *Ultrasonic Bioinstrumentation*. John Wiley & Sons, Ltd, 1988.

[29] R. J. McGough, T. V Samulski, and J. F. Kelly, “An efficient grid sectoring method for calculations of the near-field pressure generated by a circular piston,” *J. Acoust. Soc. Am.*, vol. 115, pp. 1942–1954, 2004.

CHAPTER 5

CONCLUSION

5.1 Summary

This work investigated the status of acoustic power transfer systems (APTS) for implantable medical devices (IMDs) in terms of the plate and diaphragm acoustic transducer architectures and current APTS modeling techniques. It also presented a comparative study of the plate and diaphragm, developed a modeling technique to model the effects of Depth, Orientation and Alignment via Ray Tracing (DOART), and provided a nondimensional analysis of depth, orientation, and alignment in acoustic power transfer systems.

Chapter 1 investigated the use of plate and diaphragm architectures used in literature. The study found that the majority of publications use the plate. This motived a comparative study of the plate and diaphragm in terms of power transfer potential. Also investigated were modeling techniques used in literature to design APTS. The investigation found that the majority of APTS designers use basic equations, circuit models, and 2D finite element analysis (FEA). None of these techniques are able to model the effects of orientation and alignment. 3D FEA is capable of modeling orientation and alignment, but comes at a steep computational cost and is therefore rarely used. This motivated the development of the DOART modeling technique to enable modeling of orientation and alignment while reducing the computational cost by two orders of magnitude. Further investigation revealed that as a result of the difficulty in modeling orientation and alignment, the sensitivity of power delivered to the IMD to orientation and alignment has not been investigated. This finding motivated a nondimensional study of depth, orientation, and alignment.

Chapter 2 presented a comparison of the plate and diaphragm transducers in terms of power transfer potential as a function of depth, diameter, and aspect ratio. Analytical expressions for acoustic radiation loss and viscous drag damping were combined into an equivalent resistor circuit component for the plate and diaphragm. A simulation comparison of the plate and diaphragm using circuit equivalent models found that the diaphragm is able to generate more power than the plate and is less susceptible to power loss as a function of depth for submillimeter sizes. This is strongly due to its lower operating frequency. For the low millimeter size range, the plate and diaphragm are comparable in terms of power transfer potential with the plate gaining the definite upper hand at larger sizes.

Chapter 3 presented the development of the DOART modeling technique. DOART was developed by combining circuit equivalent models, a modified version of Huygens principle, and ray tracing. The Reflected Grid Method was developed to robustly create a uniformly spaced grid on the RX face for pressure rays emitted from the TX that experience an arbitrary number of reflections. The method applies the secant root finding method to a compact series solution in order to find the initial direction that each pressure ray must be emitted from the TX in order to create the uniformly spaced grid. The method also provides information needed to calculate the reflection coefficient for each pressure ray at each point of reflection. DOART computation time and convergence were investigated. DOART computation time was found to be on the same order of magnitude as 2D FEA and one to two orders of magnitude faster than 3D FEA.

Chapter 4 presented a nondimensional analysis of depth, orientation, and alignment. Dimensional analysis for each load, frequency, diameter, depth, orientation, and alignment were first presented. Four types of design graphs were developed: depth magnitude, depth fluctuation, half angle, and half offset. The depth magnitude design graph gives the DC signal of the load voltage and power vs. depth data which is an approximation of pressure on the RX with zero reflections. The depth fluctuation design graph gives the AC signal of the load voltage and power vs. depth data which is an approximation of the pressure on the RX due to reflections only. The half angle design graph gives the angle at which the RX must be misoriented in order to reduce voltage and power by half. The half offset design graph gives the offset at which the RX must be misaligned in order to reduce voltage and power by half. The design graphs were presented in nondimensional form and correctional scaling factors given.

Using nondimensional design graphs, APTSs for IMDs can be designed to provide a specified load voltage and power and be robust against voltage and power fluctuations from disturbances in RX depth, orientation, and alignment by choosing a low operating frequency and a RX diameter that is small relative to the TX diameter. For example, using the nondimensional graphs presented in Chapter 4, if a RX requires 100 μW and 0.5 V_{RMS}, the minimum TX and RX diameters can be found by assuming a fixed RX depth. For a RX at 20 mm depth, the minimum RX diameter such that the RX thickness does not exceed the RX diameter is 43% of the TX diameter for a nondimensional frequency (Frequency*) of 3. At this frequency, the minimum usable TX diameter is 5.5 mm and has a half offset of 4.67 mm and 3.3 mm and a half angle of 40° and 27° for voltage and power, respectively. For a nondimensional frequency of 6, the minimum RX diameter is 21% of the TX diameter. The minimum TX diameter is 9.5 mm and has a half offset of 2.61 mm and 1.8 mm and a half angle of 43° and 31° for voltage and power, respectively. For a nondimensional frequency of 9, the minimum RX diameter is 14% of the TX diameter. The minimum TX diameter is 7.5 mm and has a half offset of 1.77 mm and 1.23 mm and a half angle of approximately 47° and 33° for voltage and power respectively. Of the three frequencies, the lowest frequency design is the least sensitive to offset disturbances, the most sensitive to angle disturbances, and is the most limited on the RX size with 2.36 mm being the smallest RX diameter. The highest frequency design is the most sensitive to offset disturbance, the least sensitive to angle disturbance, and allows for the smallest RX size at 1.05 mm diameter. Generally, a low operating frequency decreases absorption in the tissue and decreases sensitivity to offset disturbances. A small RX diameter decreases sensitivity to depth and angle disturbances. The choice of which design to ultimately choose is application dependent.

5.2 Contributions

In addition to the contributions stated in the summary, this work contributes the following to the field of APT for IMDs:

1) Analytical relationships for an equivalent circuit resistor component for the plate and diaphragm circuit equivalent models that account for acoustic radiation losses and viscous drag damping.

2) Simulation data comparing the power transfer potential of the plate and diaphragm transducers in terms of depth, diameter, and aspect ratio. These finding provide a guideline of when the diaphragm should be considered for use as the RX. Experimental agreement with transducer circuit equivalent models utilizing the derived resistor circuit was demonstrated prior to generating simulation data.
3) Reflected Grid Method comprised of compact series solutions to create a uniformly spaced grid on the RX for an arbitrary number of reflections.
4) DOART modeling technique and method of implementation in the form of a Matlab app. The app is an extensible tool for researchers to quickly simulate their acoustic power transfer systems. Currently, the majority of researchers are using basic equations, circuit models, and 2D FEA analysis to optimize their system in terms of depth, frequency, and sometimes diameter. 3D FEA is rarely used because of its steep computation time. This app is a step towards moving the community past the basic system modeling hurdle. Agreement of the DOART modeling technique with experimental data from two different sets of transducers was demonstrated.
5) Four types of design graphs to aid APTS designers in the development of APT for IMDs. These graphs provide a quick view of the magnitude and fluctuation of the transferred power and generated voltage, and the disturbance in orientation and alignment that will cause the RX to lose half of the transferred power and generated voltage compared to when the RX is perfectly aligned and oriented.
6) Twelve nondimensional pregenerated design graphs. These graphs represent achievable transferred power and generated voltage by APTSs and can be used by researches to gauge what is possible on the low end. It should be noted that these

graphs do not represent a maximum theoretical limit and that higher power levels can be achieved by employing complex impedance matching, more efficient transducers, and/or sophisticated power conditioning schemes.

5.3 Future Work

Future work includes the following:

1) Extending the capabilities of the DOART modeling technique. Specific features that can be developed include:
    - Derivation of the Reflected Grid Method for focused transducers.
    - Derivation of the Reflected Grid Method for multiple homogenous medium layers with variable thickness. For example, the TX could be in contact with a layer of water of z_1 thickness which could be in contact with a layer of skin of z_2 thickness which could be in contact with a layer of fat of z_3 thickness which could be in contact with the RX.
    - Support for the diaphragm as a TX. This involves calculating the emitted pressure at each point on the TX diaphragm face by calculating the deflection profile of the diaphragm as a function of radius. The current method that supports the plate as a TX assumes that the pressure on the TX face is uniform.
    - Support for various shapes of planar transducers. This involves derivation of an equivalent circuit model for the transducer and defining ray-straying areas according to the shape of the transducer (no re-derivation of the Reflected Grid Method is required).

  - SPICE or Simscape connectivity to enable modeling of complex circuit models attached to the APTS.

2) Future work with the piezoelectric plate and diaphragm include:
   - Development of a MEMS process to fabricate diaphragms that allow for deeply implantable millimeter and submillimeter size IMDs.
   - Experimental data for small diaphragm devices
   - Further studies on the repeatability of experimental data obtained for the plate and diaphragm.
   - Tests and simulation of plate and diaphragm transducers with tissue phantoms.
3) A study of how IMDs migrate in tissue would be beneficial for the design of APTS for IMDs. Relevant information would include:
   - Migration of IMD position as a function of time.
   - Statistical data of changes in IMD depth, orientation, and alignment, due to human interaction, when the IMD is implanted in tissue and a human is positioning the TX.

APPENDIX

COMBINED EFFECTS OF ORIENTATION AND ALIGNMENT

Chapter 4 illustrates the sensitivity of the voltage and power delivered to the RX load due to disturbances in RX orientation and alignment. These effects are analyzed separately with the caveat that they cannot be linearly superimposed. This appendix presents additional simulation data to illustrate the effect of combined orientation and alignment disturbances. It is important to note that positive offset indicates movement in the negative y direction and angle is rotation about the positive x axis where the positive z axis is the direction of acoustic propagation from the TX as described in Chapter 3. Figure A-1 presents voltage and power angle profiles for a 10-mm-diameter TX operating at 939.6 kHz and a 10-mm-diameter RX at a depth of 14.58 mm (Rayleigh distance). For convenience, the APTS is equivalent to the system analyzed in Chapter 4. Each line represents a RX offset from 0 mm (dark blue) to 15 mm (red). Figure A-2 presents the same data for a 5-mm-diameter RX and Figure A-3 presents the same data for a 1-mm-diameter RX. In the figures, the angle profiles decrease in magnitude and become asymmetric about 0° as RX offset strays from zero. It is also notable that the angle profile magnitude decreases more rapidly for smaller diameter RX than the larger diameter RX as offset is increased. This is a trade-off for the flatter angle profiles of the smaller diameter RX.

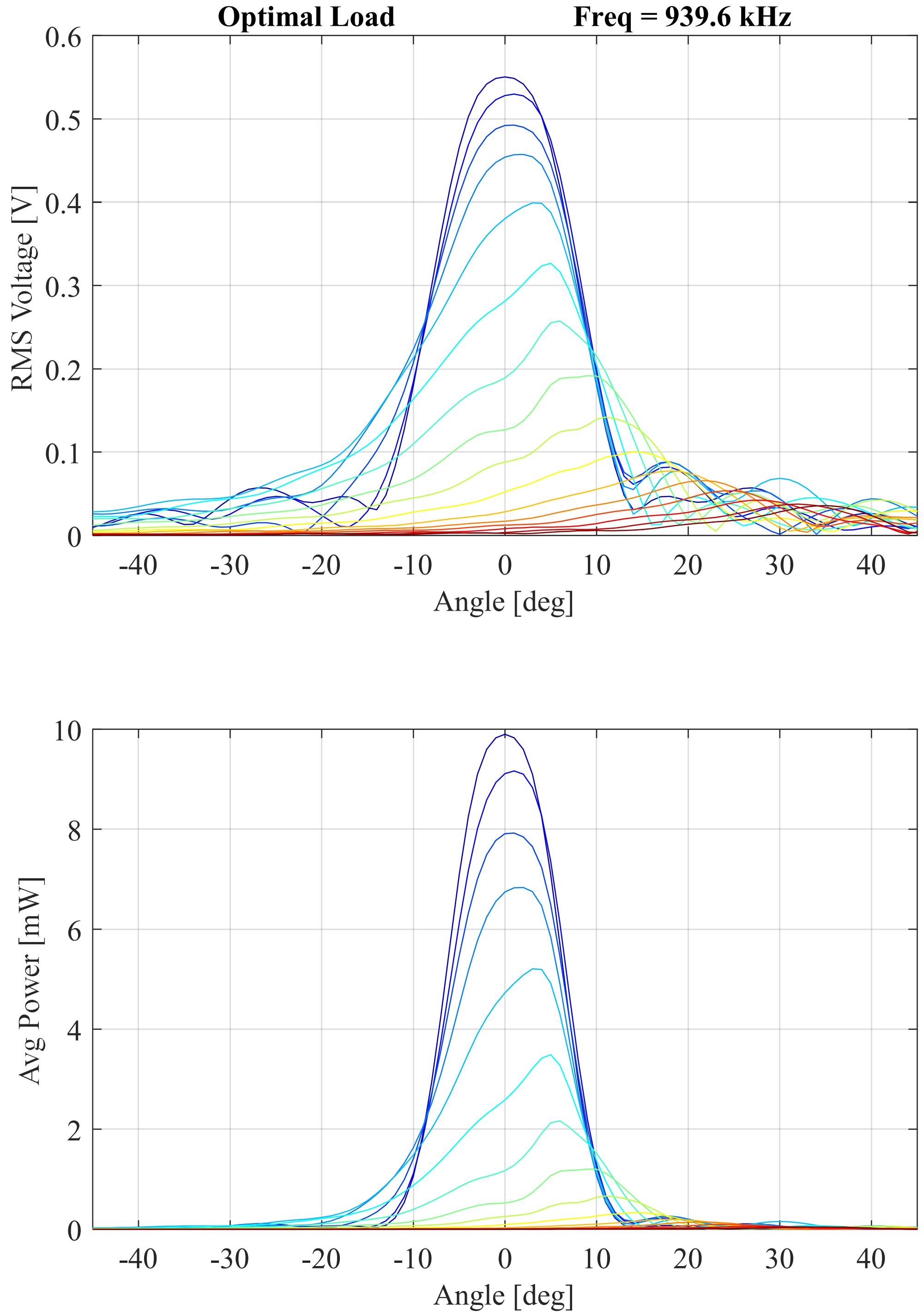

Figure A-1. RMS voltage and average power delivered to the load of a 10-mm-diameter RX as a function of RX angle for a TX and RX operating at 939.6 kHz. The emitted intensity from the 10-mm-diameter TX face is 7200 W/m^2 and the RX is placed at a depth of 14.58 mm (Rayleigh distance) and assumes a fixed-average optimal load. Each line represents a RX offset from 0 mm (dark blue) to 15 mm (red).

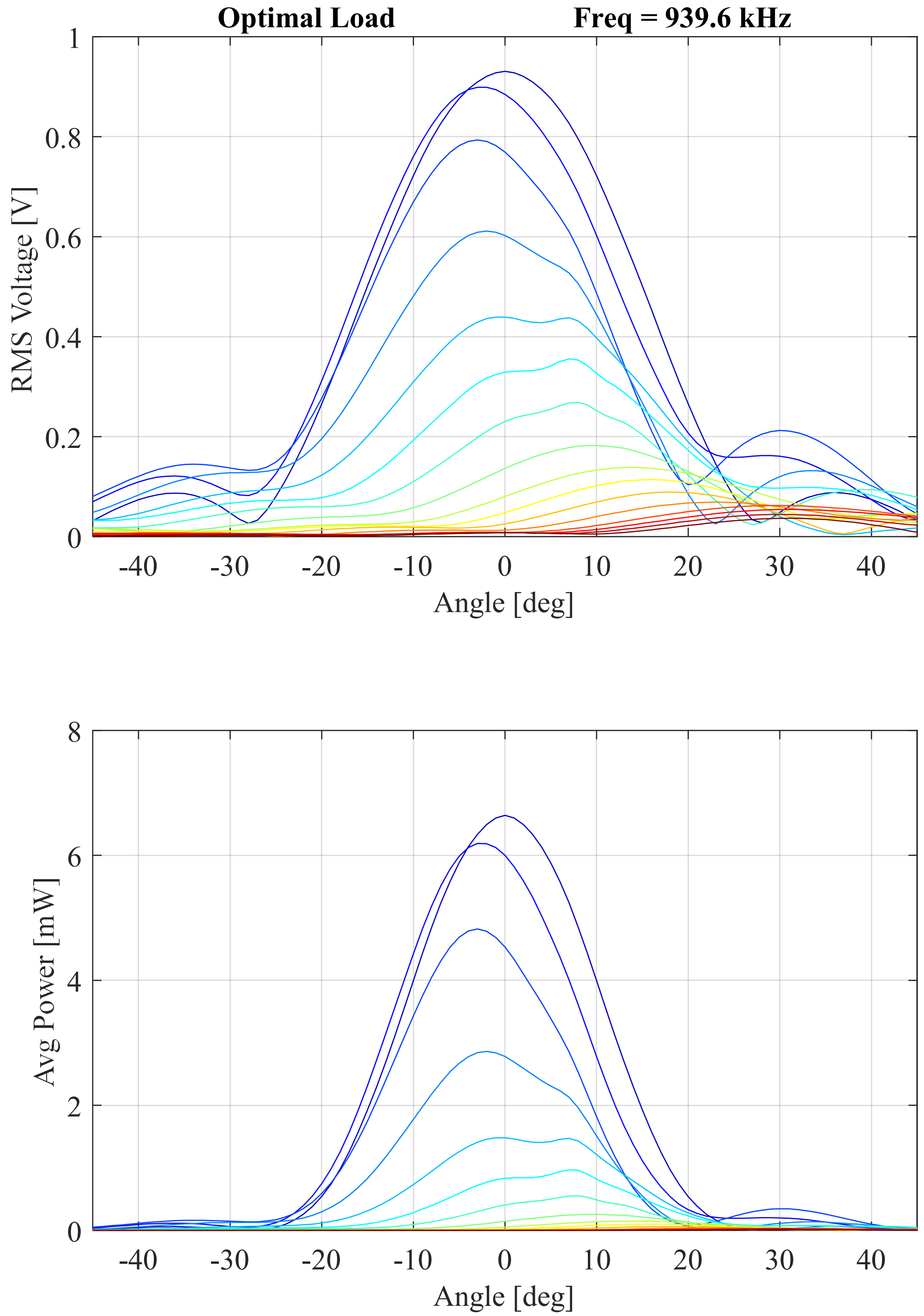

Figure A-2. RMS voltage and average power delivered to the load of a 5-mm-diameter RX as a function of RX angle for a TX and RX operating at 939.6 kHz. The emitted intensity from the 10-mm-diameter TX face is 7200 W/m^2 and the RX is placed at a depth of 14.58 mm (Rayleigh distance) and assumes a fixed-average optimal load. Each line represents a RX offset from 0 mm (dark blue) to 15 mm (red).

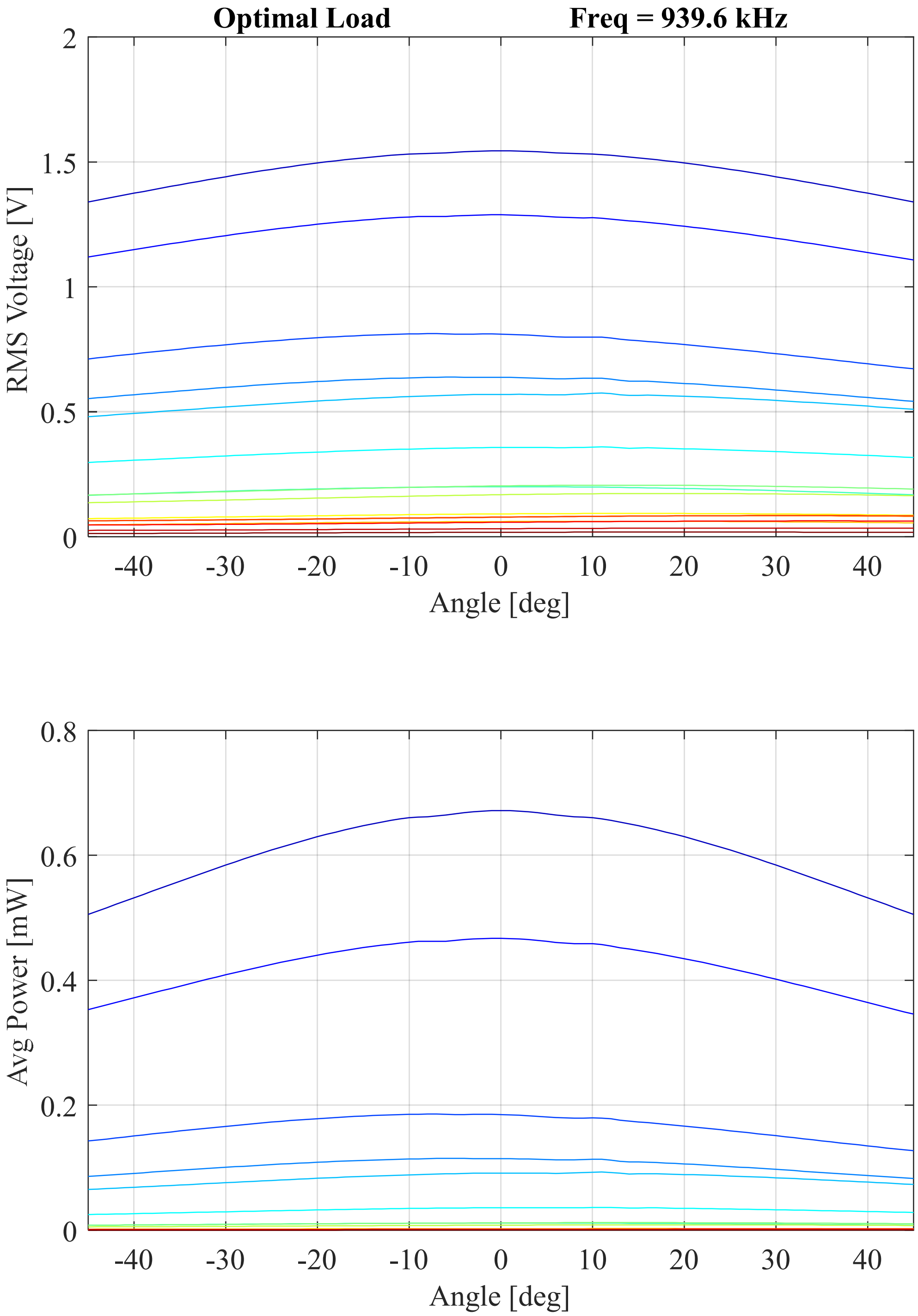

Figure A-3. RMS voltage and average power delivered to the load of a 1-mm-diameter RX as a function of RX angle for a TX and RX operating at 939.6 kHz. The emitted intensity from the 10-mm-diameter TX face is 7200 W/m^2 and the RX is placed at a depth of 14.58 mm (Rayleigh distance) and assumes a fixed-average optimal load. Each line represents a RX offset from 0 mm (dark blue) to 15 mm (red).